Charles University

Faculty of Mathematics and Physics

BACHELOR THESIS

2024 **Lukáš Frk**

FACULTY
OF MATHEMATICS
AND PHYSICS
Charles University

BACHELOR THESIS

Lukáš Frk

Study of phase transitions in models with itinerant and localized particles via machine learning

Department of Condensed Matter Physics

Supervisor of the bachelor thesis: RNDr. Martin Žonda, Ph.D.

Study programme: Physics

Specialization: None

Prague 2024

I declare that I carried out this bachelor thesis independently, and only with the cited sources, literature and other professional sources.

I understand that my work relates to the rights and obligations under the Act No. 121/2000 Coll., the Copyright Act, as amended, in particular the fact that the Charles University has the right to conclude a license agreement on the use of this work as a school work pursuant to Section 60 paragraph 1 of the Copyright Act.

In ……..... date …..... …...…….

I would like to thank my supervisor, RNDr. Martin Žonda, Ph.D., for accepting me as his student, for his guidance through the subject of machine learning and for his valuable advice concerning this study.

I must also thank all the past and present scientists, whose great discoveries contributed to the vast fountain of knowledge of humanity, and without whom this study would not be possible to make.

Finally, I would like to thank my family for their unconditional support.

Title: Study of phase transitions in models with itinerant and localized particles via machine learning

Author: Lukáš Frk

Department / Institute: Department of Condensed Matter Physics

Supervisor: RNDr. Martin Žonda, Ph.D., Department of Condensed Matter Physics

Abstract:

Phase diagrams in condensed-matter physics are often very complex. The development of methods that can identify distinct phases without any prior knowledge is, therefore, of great interest. In this study, we applied unsupervised machine learning methods to find phase boundaries in the Falicov-Kimball model, using principal component analysis and the prediction-based method. We showed that both methods can distinguish the ordered from the disordered phase. Moreover, these methods are able to distinguish the weakly localized phase from the Anderson insulator phase, which both exist within the disordered phase.

Keywords: prediction-based method, principal component analysis, Falicov-Kimball model, unsupervised phase classification, Machine Learning

Název práce: Studium fázových přechodů v modelech s itineratními a lokalizovanými částicemi pomocí strojového učení

Autor: Lukáš Frk

Katedra: Katedra fyziky kondenzovaných látek

Vedoucí bakalářské práce: RNDr. Martin Žonda, Ph.D., Katedra fyziky kondenzovaných látek

Abstrakt:

Fázové diagramy ve fyzice kondenzovaných látek jsou často velmi komplexní. Vývoj nových metod, které mohou identifikovat rozdílné fáze bez jakýchkoliv předchozích znalostí je proto velmi důležitý. V této práci jsme aplikovali metody strojového učení bez dozoru, abychom našli fázové hranice ve Falicov-Kimballově modelu, za použití analýzy hlavních komponent a metody založené na předpovědi. Ukázali jsme, že obě metody umí rozlišit uspořádanou fázi od fáze neuspořádané. Navíc jsou tyto metody schopny rozlišit slabě lokalizovanou fázi od fáze Andersonova izolátoru, které obě existují uvnitř neuspořádané fáze.

Klíčová slova: metoda založená na předpovědi, analýza hlavních komponent, Falicov-Kimballův model, klasifikace fází bez dozoru, strojové učení

Contents

1. Introduction 2
1.1. State of the art 3
1.2. Outline of our research 4
2. Model and Methods 6
2.1 Falicov-Kimball model 6
2.2 Data generation 8
2.2.1 Monte Carlo method for data generation 8
2.3 Principal component analysis 9
2.4 PCA Eigenpictures 12
2.5 Isometric feature mapping 13
2.6 Prediction-based method 13
2.7 Predictors 14
2.7.1 Neural Network basics 14
2.7.2 Simple neural network 18
2.7.3 Modified SENet neural network 18
2.7.4 Random Forest 18
3. Results 20
3.1 Principal component analysis 20
3.1.1 Simple PCA 20
3.1.2 PCA – Difference between explained variance ratios 25
3.1.3 PCA Eigenpictures 26
3.2 Isometric feature mapping – Results 31
3.2.1 Simple Isometric feature mapping 31
3.2.2 Isomap + Eigenenergies 33
3.3 Prediction-based method – Results 35
3.3.1 Simple neural network (SNN) 35
3.3.2 Modified SENet neural network 41
3.3.3 Random Forest 44
3.3.4 Random Forest on PCA 48
4. Discussion 51
5. Conclusion and outlook 53
Bibliography 55
A Attachments 61
A.1 The non-interacting Falicov-Kimball model 61
A.2 The staggered potential for the Falicov-Kimball model 63

1. Introduction

An exciting new field of study has emerged in recent decades. Machine learning has only just begun to influence everyday aspects of our lives and its impact has already been immense. The potential for its application is vast, including a plethora of scientific disciplines. And condensed-matter physics is no exception in this regard.

Materials studied in condensed-matter physics, such as strongly correlated electron systems, typically have extremely complex phase diagrams [1, 2]. Moreover, the identification of distinct phases is a very complicated problem since the way in which to choose order parameters may not always be obvious. It happens that new phases are found even in materials or models that have already been investigated for decades [1, 3, 4]. Such was the case of the Anderson Insulator (AI) phase in the Falicov-Kimball model [5]. Sometimes, the information about the new phase may even be present in the old data, yet a conventional analysis may overlook it [6].

The development of techniques capable of distinguishing distinct phases in these materials is therefore of a paramount importance in condensed-matter physics [7, 8, 9]. The rapid progress in machine learning (ML) methods and data analysis has led to the existence of methods and techniques that aim to do exactly that. Ideally, these methods should be unsupervised, meaning that they do not require any prior knowledge about the correct phase diagram. Because that way, we can discover new phases that were not discovered before.

With exponential increase in memory and computing power that has been going on for several decades now, big datasets are readily available in many areas of modern science. As a result, data analysis has become an important part of a great number of research fields, including experimental particle physics, cosmology, quantum computing or biophysics. Experiments such as ATLAS and CMS at the LHC in CERN or cosmology projects like Sloan Digital Sky Survey are just a few examples of using big datasets and data analysis methods in modern science. Furthermore, ML and data science have also become key stones in many aspects of modern technology, such as image recognition, natural language processing, medical diagnostic [10], self-driving cars, biotechnology or smart devices [11].

Recently, ML methods have started to become widely implemented in condensed-matter physics as well, although there have already been some isolated applications of machine learning in years prior. Together with Monte Carlo [12, 13, 14] data, ML methods have been used in recognizing phase transitions [15, 16, 17, 18, 19, 20] or to explore overcoming the sign-problem bottleneck [18].

Both learning from labeled data (supervised learning) [15, 21], as well as learning from unlabeled data (unsupervised learning) [16] have been successfully applied in condensed-matter physics. The latter approach is especially appealing since it can be used to find patterns and structures without any prior knowledge about the underlying physics.

However, there are still challenges ahead. The ML methods are not always capable of finding all phase transition boundaries, as was evident from the article by Richter-Laskowska et. al [22]. In this article, learning by confusion (LBC) method was applied to several different models, including the Falicov-Kimball model. Although the method was able to find the critical temperature for the continuous phase transition, it had problems finding it for the discontinuous phase transition. The critical temperature for the discontinuous phase transition was correctly determined for the Blume-Capel and the q-state Potts models, but not for the Falicov-Kimball model [22]. This shows that even though ML methods perform good, they still do not always work ideally and it is therefore important to improve this methods or to develop new and better ones.

1.1. State of the art

One of the main objectives of many researchers in the field of condense-matter physics is to develop algorithms that are capable of learning from data automatically. There have been quite a lot of ML techniques introduced, some of which were even successful to a lesser or greater extent. Here we focus on methods relevant to this study with the most important ones being later discussed in detail.

One of them is learning by confusion (LBC), which was recently proposed in [17]. This approach utilizes methods of supervised learning in a clever way that allows it to make predictions without any prior knowledge about the data. The key is to label some of the data deliberately incorrectly, which leads to the confusion of the predictor, hence the name. Based on the amount of incorrectly labeled data, the predictor´s performance is better or worse, which can be used to discern correct labelling. This proved to be useful in determining the critical temperature of phase transitions without any prior knowledge, as has been done in [22].

However, this approach is not without its difficulties, as it was recently shown for the Falicov-Kimball model [22]. In general, phase transitions are classified into two main classes, namely discontinuous (first-order) and continuous (second-order). Although learning by confusion is capable of finding the critical temperature for the continuous phase transition, finding it for the discontinuous phase transition depends on the system, as has been demonstrated in [22], where the discontinuous phase transition was found for the Blume-Capel and the q-state Potts models, but not for the Falicov-Kimball model.

Another example of an effective approach was the divergent vector field method, also called the prediction-based method. In this method, the difference between true parameters of the examined model and parameters inferred from some properties of the system is used to identify phase boundaries. This method was introduced in [23], where it was applied to the two-dimensional Ising model in equilibrium, and the dissipative Kuramoto-Hopf model out of equilibrium. This method was also successfully applied to several problems, such as symmetry-breaking [23] or quantum, and topological phase transitions [24] in various systems.

The mean-based method, which was introduced in [6], is another great way of tackling the phase classification problem. This method builds on the prediction-based method mentioned above. The advantage of the mean-based method is that it, unlike other methods mentioned before, does not rely on a black-box predictive technique. Instead, it uses the difference between mean input features as an indicator for phase transitions [6]. As a result, it is computationally cheap and directly explainable.

Principal component analysis (PCA) is a standard method used for dimensional reduction of the input data in ML. Nevertheless, it was recently shown that it can be utilized for an unsupervised investigation of phase transitions. In particular for studying phase transitions in the Ising, Blume-Capel, BSI and XY models [25]. This method is useful even if no obvious order parameter is present since it can bring out the subtle ones. This was the case for triangular-lattice Ising model (TLIM), as shown in [25]. The evolution of the principal component distribution can be used to distinguish between continuous and discontinuous phase transitions, which was also shown in [25].

A plethora of phenomena is commonly investigated using the Falicov-Kimball model, such as crystallization [26, 27, 28], metal-insulator and valence transitions [29, 30] or nonlocal correlations [31, 32, 33, 34]. Also, thanks to its relative simplicity, this model has become a standard for the development of new methods for identifying phase transitions and distinguishing different phases in the context of strongly correlated systems [35, 36, 37, 38, 39, 40, 41, 42, 43, 44] and recently machine learning [41, 45].

Unsupervised prediction-based methods built on deep learning, as well as the mean-based method (both already mentioned in the text above) have recently been applied to the Falicov-Kimball model to find phases in its rich ground-state phase diagram [6]. Furthermore, these methods led to more general approaches [46].

The aforementioned learning by confusion method was also applied to the Falicov-Kimball model [22], however it did not perform sufficiently well on this model, as it was not capable of finding the discontinuous phase transition in this model.

In this study, we show that several unsupervised methods, including methods that are simpler than LBC, can be used to correctly identify the phase transition boundary between the ordered and the disordered phase of the Falicov-Kimball model irrespective of the type of the phase transition. Moreover, some of these methods can also find other phase transition boundaries, namely the boundary between the weakly localized phase and the Anderson insulator phase.

1.2. Outline of our research

In our study we investigate the phase diagram of the Falicov-Kimball model, which describes a correlated electron system on a two-dimensional lattice and will be introduced in detail in the next chapter. This model is well known for its complicated phase diagram and as such presents a great test bed for the ML classification techniques.

We focus on three main techniques: principal component analysis (PCA), isometric feature mapping (Isomap) and the prediction-based method, which will all be described in further detail in the Model and Methods chapter. All of these methods were applied to the Falicov-Kimball model, which is one of the standard models in condensed matter physics, also used for example in [6, 22, 23, 47]. The main advantage of this model is its relative simplicity, which is utilized for the development of new methods for identifying phase transitions and distinguishing different phases.

Two different convolutional neural networks (CNNs) and one random forest regressor were used in this study as a predictor for the prediction-based method. All predictors are described in the Predictors subchapter (2.7 Predictors).

The primary results of this study are: The ordered and the disordered phase in the Falicov-Kimball model are readily distinguishable when performing principal component analysis and the correct phase boundary can be easily found this way. Furthermore, the phase transition boundary between the weakly localized phase and the Anderson insulator phase (the WL-AI boundary for short) can be found using the PCA method as well.

Isometric feature mapping (Isomap) can be used in a similar way as PCA to distinguish the ordered and the disordered phase two phases as well. Crucially, Isomap in combination with eigenenergies of electron configurations is capable of distinguishing the weakly localized phase and the Anderson insulator phase.

Finally, the prediction-based method performed great in finding the phase boundary between the ordered and the disordered phase in the Falicov-Kimball model for several different predictors (neural networks or random forest regressor). This method was also capable of finding hints of the boundary between the WL and AI phases, although it was not as clear cut as the boundary between the ordered and the disordered phase.

2. Model and Methods

2.1 Falicov-Kimball model

A physical system examined in this study was a two-dimensional spinless Falicov-Kimball model (FKM). Originally proposed to explain the metal-semiconductor transition in SmB_6 and metal oxides [48], it is one of the simplest models used to describe interaction of correlated electrons with heavy localized particles.

The main advantage of FKM comes from its accessibility by exact methods, because it is solvable exactly in the limit of infinite dimensions using dynamical mean-field theory (DMFT) [35, 44, 49, 50]. And in finite dimensions, it can be addressed by an exact, sign-problem-free Monte Carlo (MC) method [41, 42, 43, 51]. This is possible thanks to the fact that in the FKM, both quantum and classical degrees of freedom are combined [47].

Moreover, there exist several simplified cases of the Falicov-Kimball model, which can be solved analytically even in finite dimensions. Examples of these cases include the non-interacting case ($U = 0$) and the staggered potential ($U = \Delta \sum_l (-1)^l n_l$, where n_l is the occupancy of the lattice site l). These cases are presented in the Attachments (A Attachments) to this study (the non-interacting case is shown in the Attachment A.1, the staggered potential in the Attachment A.2)

Despite its relatively simple nature, research of this model has led to many new findings, even for the simplest spinless version of the model. For example, the interplay of topology and interaction at finite temperatures can be studied using simple generalizations of the FKM [52]. Another important result was a derivation of universal features of the critical metal-insulator transition that are transferable to other Hubbard-like models [53, 54].

The Hamiltonian of the spinless FKM at half filling is [47]:

$$H_{FK} = -t \sum_{\langle i,j \rangle} \left(d_i^\dagger d_j + d_j^\dagger d_i \right) + U \sum_i \left(f_i^\dagger f_i - \frac{1}{2} \right) \left(d_i^\dagger d_i - \frac{1}{2} \right), \qquad (1)$$

Where $d_i^\dagger (d_i)$ and $f_i^\dagger (f_i)$ are creation (annihilation) operators for light (d) particles and heavy (f) particles at lattice side i. For simplicity, from now on, we will call them f and d electrons, respectively. U is the Coulomb strength present at the site of interaction and t denotes the hopping integral. All energy values are expressed in terms of t in this study. Altogether, the first term represents a nearest-neighbor hopping of spinless d electrons on a lattice. The second term then describes a local Coulomb-like interaction between the localized f electron and an itinerant d electron on the lattice side i. The factors $-\frac{1}{2}$ in the second term are used to set the half-filling conditions [6, 47] for chemical potential $\mu = 0$.

The phase diagram of this model (see Fig. 1) consist of three main phases. The first one is an ordered charge-density wave (CDW) phase (OP), from now on

referred to as the ordered phase, that exists at low temperatures [49, 50, 51, 55, 56]. The other two main phases are disordered: a gapless disordered phase for weak interaction U and high temperatures (DPw), and a gapped disordered phase for strong interaction U and high temperatures (DPs) [35, 57]. These two disordered phases are also called a metal phase and an insulator phase [58], due to the presence of a gap in the density of states (DOS) at the Fermi level in the case of the DPs phase (insulator) and the absence of such gap in the case of the DPw phase (metal or "metallic" phase), as can also be seen from the DOS subgraphs in Fig. 1 for distinct phases.

However, the study of Antipov et al. revealed that this metal-insulator boundary may not be as clear as previously thought, because the "metallic" phase shows Anderson localization and, therefore, might be isolating in the thermodynamic limit as well [5]. At finite size, there is a smooth transition from Fermi gas at $U = 0$ through the weak localization phase to the Anderson localized phase, which all form parts of the "metallic" DPw phase. The schematic phase diagram from the cited study is also shown in Fig. 1.

The main phases were identified both for finite, as well as infinite dimensions. However, other less prominent and less understood phases are present in the phase diagram as well. For example, the gaped and gapless regimes in the ordered phase [47, 59]. These phases are not shown in Fig. 1, because their boundaries are not yet fully known for finite dimensional system.

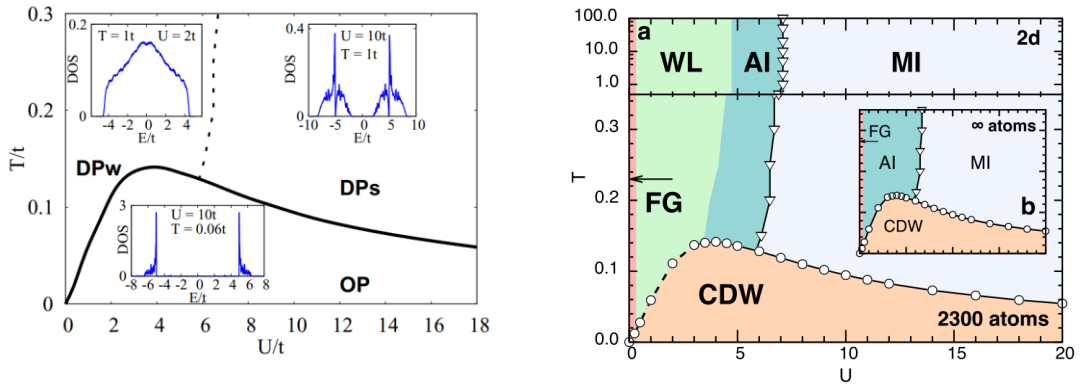

Fig. 1: Left picture: Simplified phase diagram of the spinless FK model on a square 2D lattice with the ordered CDW phase (OP) and disordered phases in weak (DPw) and strong (DPs) interaction regimes. Typical *d*-electron DOS in respective phases are also shown [6]. (Used with permission of the author).

Right picture: Phase diagram of the particle-hole symmetric FK model, consisting of different phases: Fermi gas (FG) at $U = 0$, charge-density wave insulator (CDW) at a low temperature, and all nonzero values of U. High-temperature phases: Anderson insulator (AI) at intermediate values of U crossing over to a weakly localized (WL) at smaller U, Mott-like insulator (MI) at large U. The points and lines show phase boundaries; the dashed line indicates the first-order phase transition between WL and CDW phases. Inset: Extrapolation to the thermodynamic limit.

The properties of all phases play an important role when investigating a great number of physical phenomena, including metal-insulator and valence transitions [29, 60, 61, 62, 63], or localization and correlations [5, 33, 34, 47, 53, 64, 65].

Finally, the type of phase transition in the Falicov-Kimball model depends on the U/t ratio. If the ratio is sufficiently small, the phase transition is discontinuous, whereas for interactions that are stronger than a critical value $U^*/t \approx 1$, the phase transition is continuous [22].

On top of that, the phase diagram of the Falicov-Kimball model becomes even more complex away from the half-filling [2, 66, 67]. Due to this complexity, the classification of the ground state phases was a long and difficult task that had to be done manually. This complex nature makes the model quite a challenge for unsupervised phase classification methods, but also makes it a good model to test these methods.

2.2 Data generation

The data used in this study were generated using a sign-problem-free Monte Carlo (MC) method [12, 13, 14]. This method will be explained briefly in the following subchapter. For a given combination of temperature T and potential U, 20 independent MC simulations were performed producing 20 different files. Each file consisted of 500 MC snapshots of the *f*-electron configurations and related *d*-electron densities, which were stored as row vectors. We are focusing on this type of data because it is a natural outcome of simulation. Also, this type of data can be easily accessed in some types of experiments, e.g., cold atoms trapped in optical lattices [68].

In this study, four different lattice sizes in the Falicov-Kimball model were examined. The shapes of these lattices were 6 × 6, 8 × 8, 10 × 10 and 12 × 12. For brevity, these lattices will be denoted as L6, L8, L10 and L12 in the rest of the study. Multiple configurations were generated for different combinations of potential U and temperature T. The range of the temperature was (0.005, 0.300) with step 0.005, which means that 60 different temperatures were considered in this study. The range of potential U was (0.25, 12.0) with step 0.25, meaning 48 different values of potential. The values of both U and T are expressed in terms of the hopping integral t, as was already stated in the previous subchapter.

2.2.1 Monte Carlo method for data generation

We use the fact that the *f*-particle quantum number operators n_i^f, which are defined as: $n_i^f = f_i^\dagger f_i$, are good quantum numbers with respect to the Falicov-Kimball Hamiltonian (1). Therefore, they can be replaced by their eigenvalues $f_i = 1$ or $f_i = 0$ for occupied or unoccupied site respectively. The classical MC procedure [42, 43, 51, 69] was then used to sample over the space of possible *f*-configurations.

Quantum problem for *d* electrons is solved at each MC update by exact diagonalization:

$$H_S^f(\boldsymbol{f}) = \sum_{i,j} h_{ij}(\boldsymbol{f}) d_i^\dagger d_j - \frac{U}{2}\left(N_f - \frac{L^2}{2}\right) = \sum_{\alpha} \lambda_\alpha(\boldsymbol{f}) b_\alpha^\dagger b_\alpha - \frac{U}{2}\left(N_f - \frac{L^2}{2}\right) \quad (2)$$

where $h_{ij}(\boldsymbol{f}) = U\left(f_i - \frac{1}{2}\right)\delta_{ij} - t_{ij}$ and t_{ij} are the elements of hopping matrix which are one for nearest neighbors and zero otherwise. N_f is the total number of *f* electrons and L^2 is the number of lattice sites. The unitary transformation performed after the second equal sign expresses the diagonal matrix $\lambda_\alpha(\boldsymbol{f})$ of eigenvalues (in ascending order) of the Hamiltonian $\boldsymbol{h}(\boldsymbol{f})$ for a particular *f*-electron configuration. This transformation can be written as $\boldsymbol{\lambda}(\boldsymbol{f}) = \boldsymbol{U}(\boldsymbol{f})\boldsymbol{h}(\boldsymbol{f})\boldsymbol{U}^\dagger(\boldsymbol{f})$, where $\boldsymbol{U}(\boldsymbol{f})$ is the matrix of eigenvectors.

We can calculate average occupancy of site *j* by *d*-electrons for given *f*-electron configuration from the eigenvalues and eigenvectors using the following formula:

$$\langle n_d^j(\boldsymbol{f})\rangle = \sum_{\alpha=1}^{L^2} \frac{\boldsymbol{U}_{j\alpha}(\boldsymbol{f})\boldsymbol{U}_{\alpha j}^\dagger(\boldsymbol{f})}{1 + exp[\beta\lambda_\alpha(\boldsymbol{f})]} \quad (3)$$

where $\beta = 1/T$ is the inverse temperature of MC simulation and the sum goes over all eigenvalues.

2.3 Principal component analysis

Principal component analysis (PCA) is one of the most commonly used techniques in modern data science, being employed in such diverse fields as computer graphics and neuroscience [70]. PCA serves as a dimension reduction technique and hence is a typical tool for reducing complex data sets into a lower dimension, which often helps to uncover underlying structures in data that show no obvious order. PCA performs its job by quantifying how important each dimension of the data is for describing the variance of the data set.

A very important feature of PCA is that it is non-parametric. Therefore, it can be applied to any data set without the need to adjust any parameters. This also means that the method has no regard for how the data was recorded [70].

One of the main limitations of PCA comes from the fact that it is a linear method. Although the assumption of linearity is usually useful and makes the method simple, yet effective, it also limits its applicability. Therefore, non-linear patterns in a data set cannot be found using PCA.

Another limitation of PCA is caused by assuming orthogonality of principal components. This decorrelates the data by removing second-order dependencies. However, if such dependencies exist in the original data, their removal leads to the situation where the reduced representation of the data is not optimal. A parametric approach known as *kernel PCA* can be used to solve this issue. In this approach, a prior knowledge about the problem is utilized by applying a nonlinearity (i.e., kernel)

to transform the data to the basis that is more appropriate and to which PCA can be better applied. However, since it relies on prior knowledge about the data, the kernel PCA technique was not used in this study, as our goal was to explore and utilize methods that work without any prior knowledge.

Explanation of the method: PCA works by transforming data to a new coordinate system, therefore it can be defined as an orthogonal linear transformation [71]. An easy intuition as to what PCA is comes from thinking about it as fitting a p-dimensional ellipsoid to the data, where the length of each axis of the ellipsoid describes the importance of a principal component (the longer the axis, the more important the principal component). But before fitting the ellipsoid, its center needs to be found. It is natural for the center to be 0. Therefore, to center each variable around 0, the first step of performing PCA analysis is subtracting the mean of the variable's observed values from each of those values.

Let then $\mathbf{X}$ be a $n \times p$ data matrix (with already transformed values centered around 0), where each of the p columns represents some feature and each of the n rows can be thought of as a different instance of an experiment. Here, the first of the assumption of PCA comes in play and that is linearity.

We want to find another basis, which will be a linear combination of the original basis. This new basis should be able to best describe the data set used. Let then $\mathbf{Y}$ be a new data matrix (also $n \times p$ matrix), which is a new representation of the data set. Matrices $\mathbf{X}$ and $\mathbf{Y}$ are related by an equation:

$$\mathbf{Y} = \mathbf{PX}, \tag{4}$$

where $\mathbf{P}$ is a linear transformation that was applied to matrix $\mathbf{X}$. Geometrically speaking, $\mathbf{P}$ is a rotation and a stretch that was used to transform $\mathbf{X}$ into $\mathbf{Y}$. Another way to interpret the equation above is that the rows of $\mathbf{P}$, $\{p_1,...,p_m\}$, form a new basis of vectors for expressing the columns of $\mathbf{X}$ [70].

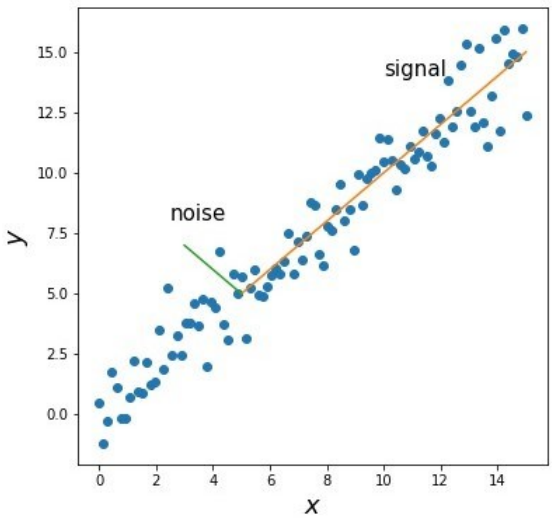

Fig. 2: An example of data having high signal-to-noise ratio (SNR).

In order to find the good choice of basis **P**, more assumptions are needed. One of these assumptions is that large variances have important structure [70]. For this assumption to be useful, we must also assume that the data has a high signal-to-noise ratio (SNR), such as is the case for data shown in Fig. 2.

This means that the data are not too noisy and that the variances are caused by the dynamics of interest. If we therefore maximize the variance (and also SNR), we find the appropriate rotation of the original basis.

Next step in performing PCA is calculating a covariance matrix. For a $m \times n$ matrix **X**, the definition of the covariance matrix is:

$$\boldsymbol{C_X} = \frac{1}{n}\boldsymbol{X}\boldsymbol{X}^{\boldsymbol{T}} \tag{5}$$

The covariance matrix may help us in deciding whether some variables are redundant or not. Because the off-diagonal terms represent the covariance between different variables, they should ideally be zero, since then the variables are not correlated and are thus not redundant. This means that the covariance matrix should be a diagonal matrix.

One way to achieve this for a matrix $\mathbf{C}_\mathbf{Y}$ which is a covariance matrix calculated from **Y**, is for matrix **P** to be an orthonormal matrix, which is exactly what PCA assumes it to be. Then, the rows of **P**, $\{p_1,...,p_m\}$ are the principal components, provided they are also ordered in such a way that the dimensions of **Y** are rank-ordered according to variance. This rank-ordering aids us in determining the importance of each principal direction.

As a side note, principal component analysis is closely related to another matrix factorization method, the singular value decomposition (SVD), as we only briefly show here. If we define the aforementioned matrix **Y** as: $\boldsymbol{Y} = \frac{1}{\sqrt{n}}\boldsymbol{X}^{\boldsymbol{T}}$, then:

$$\boldsymbol{Y}^{\boldsymbol{T}}\boldsymbol{Y} = \left(\frac{1}{\sqrt{n}}\boldsymbol{X}^{\boldsymbol{T}}\right)^{T}\frac{1}{\sqrt{n}}\boldsymbol{X}^{\boldsymbol{T}} = \frac{1}{n}\boldsymbol{X}\boldsymbol{X}^{\boldsymbol{T}} = \boldsymbol{C_X} \tag{6}$$

Calculating SVD of **Y** gives us: $\boldsymbol{Y} = \boldsymbol{U}\boldsymbol{\Sigma}\boldsymbol{V}^{\boldsymbol{T}}$, where the columns of **V** contain the eigenvectors of $\boldsymbol{Y}^{\boldsymbol{T}}\boldsymbol{Y} = \boldsymbol{C_X}$. The matrix $\boldsymbol{\Sigma}$ has the variance of data $\boldsymbol{\sigma}^2$ on its main diagonal. Since the principal components of **X** are the eigenvectors of $\boldsymbol{C_X}$ as was mentioned earlier, the columns of **V** are the principal components of **X**. Therefore, finding the principal components is equivalent to finding an orthonormal basis that spans the column space of our original data matrix **X** [70].

Finally, it is worth noting that in the case of the Falicov-Kimball model, which was examined in this study, the explained variance ratio of the first component (termed the first explained variance ratio for brevity in any further text) plays the role of the order parameter. The explained variance ratio is the explained variance divided by the sum of all explained variances and is therefore normalized to one.

Therefore, in the ordered phase, the first component explains almost everything and the first explained variance ratio is almost 1, and in the disordered phase, all components are important and so the first explained variance ratio goes to zero. Hence, the first explained variance ratio plays the role of the order parameter.

Furthermore, the explained variance ratio of the second component (the second explained variance ratio) plays the role of susceptibility.

2.4 PCA Eigenpictures

The idea behind this approach is that we can imagine that configurations for different U and T values are images of different faces and face recognition techniques can be performed on them.

It was shown by Sirovich and Kirby that PCA can be applied to create a set of basis features given a collection of face images [72]. These basis feature create basis images (also called eigenpictures) of the given collection of face images. Therefore, a linear combination of the basis images can reconstruct the original images in the collection. An example of eigenpictures of face images is shown in Fig. 3.

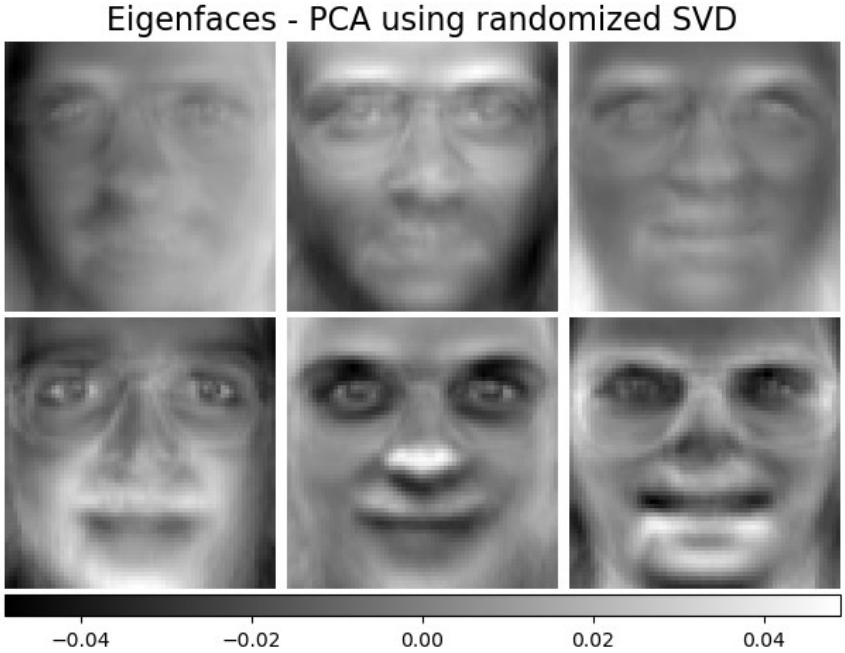

Fig. 3: An example of eigenpictures of face images [73]. These eigenpictures were created from The Olivetti faces dataset [74].

Since our data represent snapshots of *f*-electron configurations and related *d*-electron densities on a 2-dimensional lattice, it is possible to reshape each snapshots into a 2-dimensional L times L array, where L is the size of the lattice. The snapshots can be therefore thought of as images (of electron configurations) with L times L pixels.

Therefore, basis images of electron configurations that could reconstruct our original configurations can be created in the same way as if we had a collection of face images.

2.5 Isometric feature mapping

Isometric feature mapping (Isomap) is a non-linear dimensionality reduction technique introduced in [75]. This method builds upon the PCA method (introduced in the previous section) and the multidimensional scaling (MDS) method. However, thanks to its non-linearity, the Isomap method is capable of finding patterns in the data that these linear methods are not able to discover [76, 77, 78]. Finally, according to its authors [75]: the Isomap algorithm "efficiently computes a globally optimal solution" and, given sufficient amount of data, "is guaranteed to converge asymptotically to the true structure."

The Isomap algorithm consists of three steps [75]: In the first step, distances in the input space between pairs of points are used to identify neighboring points on the manifold M and a neighborhood graph N is created using this information. The shortest path distances in this graph N are utilized in the second step to estimate geodesic distances between all pairs of points. In the last step, an embedding of the data in a p-dimensional Euclidean space is constructed with the aid of classical MDS.

2.6 Prediction-based method

The prediction-based method, which was introduced in [23], is a method used to identify phase boundaries. It was already successfully applied to the two-dimensional Ising model and the dissipative Kuramoto-Hopf model [23].

This method is based on using a predictor (such as a neural network) for learning parameters of the physical system depending on the state of that system. It then uses the deviation of these inferred parameters from the correct ones to predict phase transitions. This approach assumes that the predictions of the predictor will get more susceptible to the change of system parameters the closer to phase boundaries the system is. At this instant, the vector field divergence of predictions will reach its maximum, which suggests a presence of a phase transition.

One of the advantages of this method is that it is economical in computational resources, because it requires only one training procedure. Crucially, no prior knowledge concerning either correct labels or even the number of different phases is required. Furthermore, it can be applied to phase diagrams of arbitrary parameter dimension [23].

A predictor capable of resolving different phases is needed for this method to work. Unsurprisingly, increasing resolution of the predictor leads to more structure in the phase diagram being revealed. Typically, deep neural network (DNN) is used as such predictor to achieve a desired resolution. The disadvantage of DNNs is that its internal workings are usually unknown due to its hidden layers. This means that the predictor functions as a black-box model. It is also important for the predictor to be as good as possible. Therefore, we tested three different predictors, which we will discuss later in the 2.7 Predictors subchapter.

Explanation of the method: The predictor is trained in such a way that its predictions p_{pred} inferred from the state of the system minimize the expectation value of the loss function L:

$$L = |\delta p|^2 \tag{7}$$

where $\delta p = p_{pred} - p_0$ is a difference between predicted and correct labels.

If we assume that the predictor is capable of distinguishing between different phases, but not among the different states within the same phase, then the optimal choice to minimize the loss function is placing every prediction at its center of mass. As a result, prediction deviations near a phase boundary have opposite orientations. To quantify this property, the vector field divergence was introduced [23]:

$$div(\delta p) = \nabla \cdot \delta p = \sum_{n=1}^{d} \frac{\partial \delta p^{(n)}}{\partial p_0^{(n)}} \tag{8}$$

where n denotes the index of the vector and d is the dimension of the parameter space.

Local maxima of (8) will generally occur at those parameter values, where the system state is most susceptible to the change of system parameters [23]. This suggests the presence of a phase boundary at these parameters.

2.7 Predictors

Two convolutional neural networks (CNNs) were used in this study as predictors for the prediction-based method: Simple neural network (SNN) and Modified SENet neural network (SENet), which will both be described in this section. A random forest regressor was applied as another predictor for this method and will also be described in this section.

2.7.1 Neural Network basics

In this part, some basic concepts concerning neural networks that were utilized in this study will be described. If the reader is already familiar with neural networks, this subsection may be skipped.

2.7.1.1 Neural network

Artificial neural networks are ML techniques that were inspired by biological neurons [79]. Therefore, the basic unit of every neural network is called a neuron as well. Each neuron receives some input, from which it computes an internal potential z, which is a weighted sum of the input terms plus a bias term (also called threshold) [79]. Some activation function f is then applied to the internal potential, which determines the output value of the neuron. The use of activation functions ensures that a non-linear operation is performed on the input data, because without it the

neural network would just give a linear combination of its input. The formula for the output value $a_j^{(l)}$ of a j-th neuron in l-th layer is shown in (9):

$$a_j^{(l)} = f\left(z_j^{(l)}\right) = f\left(\sum_{k=1}^{n} w_{jk}^{l} a_k^{l-1} + b_j^{l}\right), \tag{9}$$

where $z_j^{(l)}$ is an internal potential of a j-th neuron in l-th layer, $w_{jk}^{(l)}$ is weight of the connection between the k-th neuron of (l-1)-th layer and the j-th neuron of the l-th layer, $b_j^{(l)}$ is the bias of the j-th neuron in the l-th layer and $a_k^{(l-1)}$ is the activation of k-th neuron in the (l−1)-th layer

Some examples of the most commonly used activation functions are Rectifier Linear Unit (ReLU), hyperbolic tangent (Tanh), Sigmoid activation function or Softmax activation function. Graphs of these activation functions are shown below in right part of Fig. 4.

Typical neural network is comprised of several layers of neurons, with each layer consisting of hundreds or thousands of individual neurons. First layer of neurons is called an input layer, last layer of neurons is called an output layer and all the layers in between are called hidden layers. An example of a neural network is shown in Fig. 4. If each neuron from every layer is connected to all neurons of the next layer, the neural network is said to be fully connected.

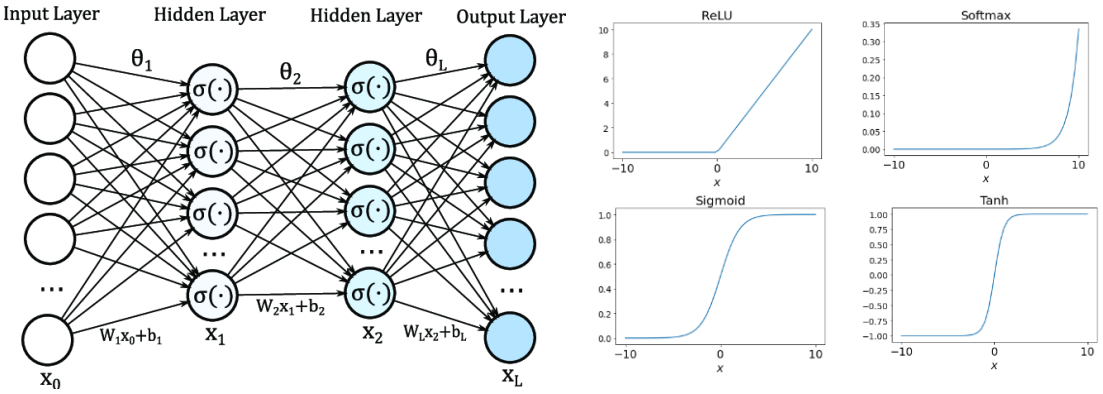

Fig. 4: Graphs of common activation functions (right)

Structure of a fully connected neural network with 2 hidden layers (left).

From “Machine Learning Tips and Tricks for Power Line Communication” by A. M. Tonello, N. A. Letizia , D. Righini, and F. Marcuzzi, *IEEE Access*, vol. 7, p. 82434-82452, 2019. doi: 10.1109/ACCESS.2019.2923321
CC BY 4.0

Weights and biases for each neuron are adjusted during the process of training the neural network in such a way that the performance of the network is optimized. The learning of neural networks happens through a process called backpropagation.

First, a forward pass is performed, when prediction $\boldsymbol{y}$ is made for each training instance x. Then, the loss function $L(\boldsymbol{y}, \hat{\boldsymbol{y}})$ is calculated. Commonly used loss function for regression problems is the mean squared error:

$$L(\boldsymbol{y}, \hat{\boldsymbol{y}}) = \frac{1}{n}\sum_{j=1}^{n}\left(y_j - \hat{y}_j\right)^2 \tag{10}$$

After the forward pass is complete, a reverse pass is made, which measures the error contribution of each connection. The derivates of the loss function L with respect to each weight and bias are calculated. First, we define error of j-th neuron in l-th layer as:

$$\delta_j^l = \frac{\partial L}{\partial z_j^l} \tag{11}$$

The error of output layer ($l = L$) is:

$$\delta_j^L = \frac{\partial L}{\partial z_j^L} = \sum_k \frac{\partial L}{\partial a_k^L}\frac{\partial a_k^L}{\partial z_j^L} = \frac{\partial L}{\partial a_j^L}\frac{\partial a_j^L}{\partial z_j^L} \tag{12}$$

We express errors δ_j^l of hidden layers in terms of errors δ_j^{l+1} of next layer:

$$\delta_j^l = \frac{\partial L}{\partial z_j^l} = \sum_k \frac{\partial L}{\partial z_k^{l+1}}\frac{\partial z_k^{l+1}}{\partial z_j^l} = \sum_k \frac{\partial z_k^{l+1}}{\partial z_j^l}\delta_j^{l+1} \tag{13}$$

Using formula for internal potential from (9), we can substitute for $\frac{\partial z_k^{l+1}}{\partial z_j^l}$:

$$\frac{\partial z_k^{l+1}}{\partial z_j^l} = w_{jk}^{l+1} f'\left(z_j^l\right) \tag{14}$$

Which gives us formula for errors of hidden layers:

$$\delta_j^l = \sum_k w_{jk}^{l+1} f'\left(z_j^l\right)\delta_j^{l+1} \tag{15}$$

This allows us to calculate the rate of change of the loss function with respect to any weight in the network:

$$\frac{\partial L}{\partial w_{jk}^l} = \delta_j^l a_k^{l-1}, \quad \frac{\partial L}{\partial b_j^l} = \delta_j^l \tag{16}$$

Where we used:

$$\frac{\partial L}{\partial w_{jk}^l} = \frac{\partial L}{\partial z_j^l}\frac{\partial z_j^l}{\partial w_{jk}^l} = \delta_j^l \frac{\partial}{\partial w_{jk}^l}\sum_i \left[w_{ji}^l a_i^{l-1} + b_j^l\right] = \delta_j^l a_k^{l-1} \tag{17}$$

Finally, using equation (16) the connection weights w_{jk}^l and biases b_j^l are changed using gradient descent method to reduce the error:

$$w_{jk}^l \leftarrow w_{jk}^l - \eta\frac{\partial L}{\partial w_{jk}^l}, \qquad b_j^l \leftarrow b_j^l - \eta\frac{\partial L}{\partial b_j^l} \tag{18}$$

where $0 < \eta \ll 1$ is the learning rate.

2.7.1.2 Convolutional neural networks (CNNs)

CNNs are another type of architecture of neural networks that in addition to previously mentioned fully connected layers use two additional layers: convolutional layers and pooling layers. These networks have been used in image recognition since 1980s [79]. A typical architecture of a sequential CNN is shown in Fig. 5. Sequential means that several convolutional and pooling layers are applied in a sequence.

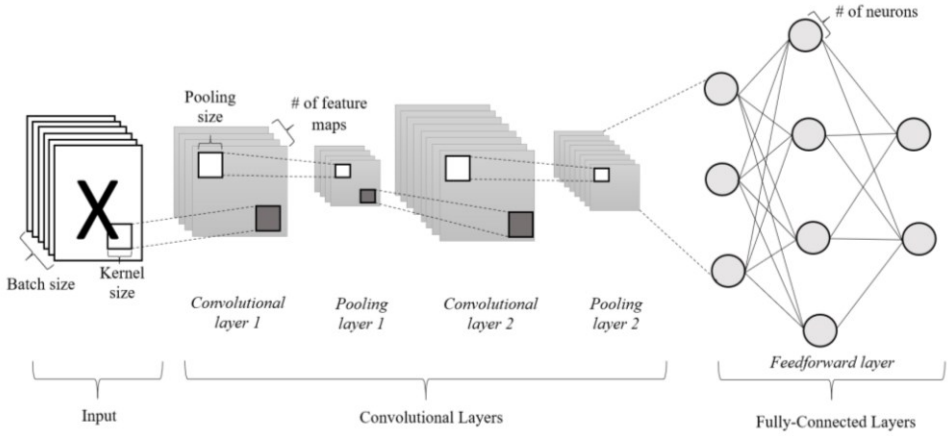

Fig. 5: Typical network architecture of a sequential CNN

From "Optimal Design of Convolutional Neural Network Architectures Using Teaching–Learning-Based Optimization for Image Classification" by Ang, K.M.; El-kenawy, E.-S.M.; Abdelhamid, A.A.; Ibrahim, A.; Alharbi, A.H.; Khafaga, D.S.; Tiang, S.S.; Lim, W.H, *Symmetry*, vol. *14*(11), p. 4, 2022. (https://doi.org/10.3390/sym14112323) CC BY

Neurons in the first convolution layer are connected only to those pixels from the input that are in their receptive field. Neurons in next convolution layers are connected in a similar way and their receptive field always corresponds to a small rectangle in the previous layer

Weights of neurons are represented by a matrix which has the size of the neuron´s receptive field. These matrices are called filters or kernels [79]. As was the case for weights and biases in the deep neural network, the weights in the kernels are learned automatically during the CNNs training.

Similarly to convolutional layers, pooling layers are also connected only to some small amount of pixels in their rectangular receptive field. The inputs of the pooling layer are combined into a single value, usually maximum or mean of the input values. This accomplishes the main goal of the pooling layer, which is to reduce the number of parameters of the neural network [79].

Following three sections describe predictors used in this study (two neural networks and one random forest regressor).

2.7.2 Simple neural network

Simple neural network is a simple convolutional neural network consisting of only four layers: a convolutional layer, two hidden dense layers and an output layer. The network starts with a convolution layer that consists of 4 filters (matrices) of the same shape, which is 1 × 2 × 2. The movement of these filters was naturally chosen to be (1,2,2) meaning that after its movement the filter did not overlap with its previous position.

Two hidden dense layers follow the convolution layer. These dense layers consist of 512 and 256 neurons. The activation function for these two layers is Rectified Linear Unit (ReLU), which is one of the standard activation functions utilized in neural networks. Also, in order to avoid overfitting, L2 regularization is introduced to both hidden layers.

The final output layer of the network consists of two neurons, which correspond to the number of features the network is supposed to predict, which is temperature T and potential U in this case. ReLU activation function is used in the output layer as well.

2.7.3 Modified SENet neural network

Squeeze-and-Excitation Network (SENet) [80] was the winning architecture of ILSVRC 2017 challenge [79], which is an annual contest aimed at creating neural networks that would excel at image classification.

Due to the fact that a typical image size is 256 × 256, but the shape of our input was significantly smaller, the SENet network had to be modified. This was done by removing last three convolution layers from the network, as each convolution layer makes its input smaller and so due to our original input being smaller in the first place, it was impossible to make it any smaller after several convolutional layers of the SENet network have already been applied.

SENet network was chosen in this study due to a part of its architecture called an SE block, which makes this network particularly suitable for our problem. The SE block analyzes exclusively the depth dimensions of the data and learns which features are typically active together [79]. In our case, the depth dimension of the input data was 2, one for f and one for d electrons configuration. Therefore, the SE block was intended to provide some information about the correlation of f and d electrons.

2.7.4 Random Forest

Random forest is one of the most powerful ML algorithms [79]. It is an ensemble of decision trees, meaning that several different decision tree classifiers are trained on different subsets of the data set and their predictions are then combined. Typically the class of the training instance chosen by majority of the decision trees is the class chosen by the random forest classifier.

Decision trees are simple ML algorithms that perform segmentation of the multidimensional data space. This simply means that they divide space into number of high dimensional rectangles. A new instance of data is classified according to the major group in its box. The set of splitting rules used for space segmentation can be summarized in a tree, hence the name of the algorithm.

Because the number of parameters is not determined prior to training, decision trees belong to a class of models called nonparametric models [79]. As a result, decision trees are likely to overfit the data. Therefore, some form of regularization is needed. There are several ways of doing that [79].

Setting the maximum depth of the tree is one of them. Another is to set the minimum number of samples in a node before it can be split or the minimum number of samples needed for a node to have in order to be created. Finally, a maximum number of nodes in a tree can be used as well.

Although we tested several different random forest regressors in our study, the main one, which was used for creating the graphs shown in the Results (3.3.3 Random Forest section) consisted of 20 decision trees with no regularization.

3. Results

3.1 Principal component analysis

3.1.1 Simple PCA

Our quest for identifying correct phases in the Falicov-Kimball model has begun with applying principal components analysis (PCA) to our data. The idea behind our approach was to discover how important the first few explained variance ratios are in describing the *f* and *d* electron configurations for a given combination of temperature *T* and potential *U*. Or in other words, how much of the information about the configuration can be explained by only these first few explained variance ratios.

To find out, we calculated a participation ratio for both *f* and *d* electrons for all possible *T* and *U* combinations. The participation ratio tells us a number *n* of the first *n* explained variance ratio components needed to describe more than *x* % of variance in the data, where *x* is some arbitrary value. We have chosen *x* to successively be 95, 90, 80 and 60 %. A graph of *n* depending on *U* and *T* for *f* electrons for L12 lattice is shown in Fig. 6. The same graph for L12 lattice, but for *d* electrons is present in Fig. 7. The percentage *x* is written in the upper left corner of each graph.

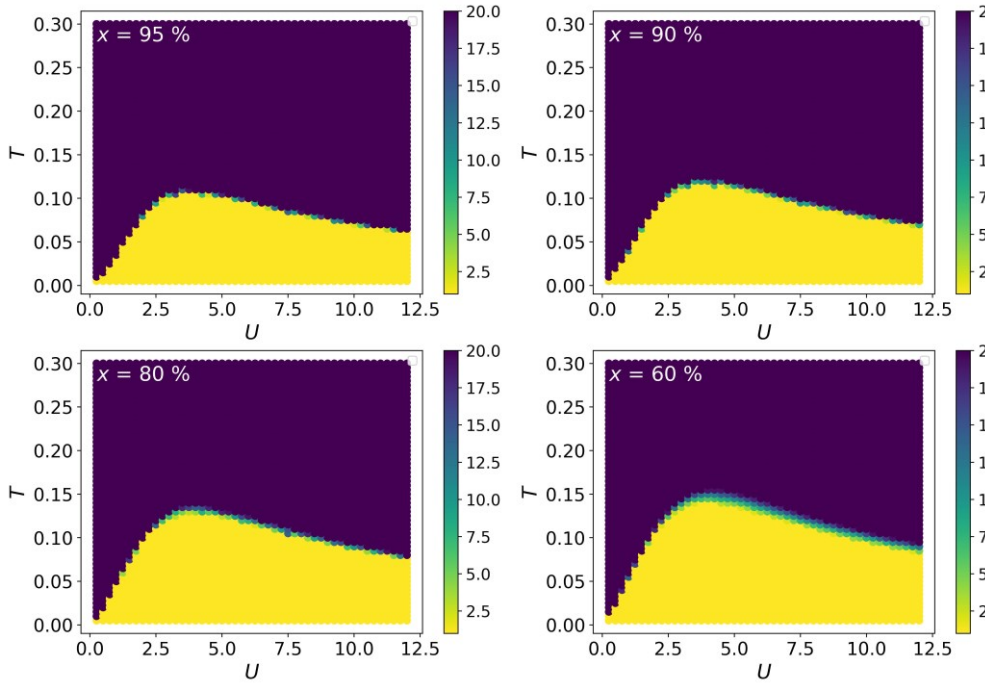

Fig. 6: The participation ratio for *f* electrons in L12 lattice. The percentage *x* of the described variance in the data is written in the upper left corner of each graph.

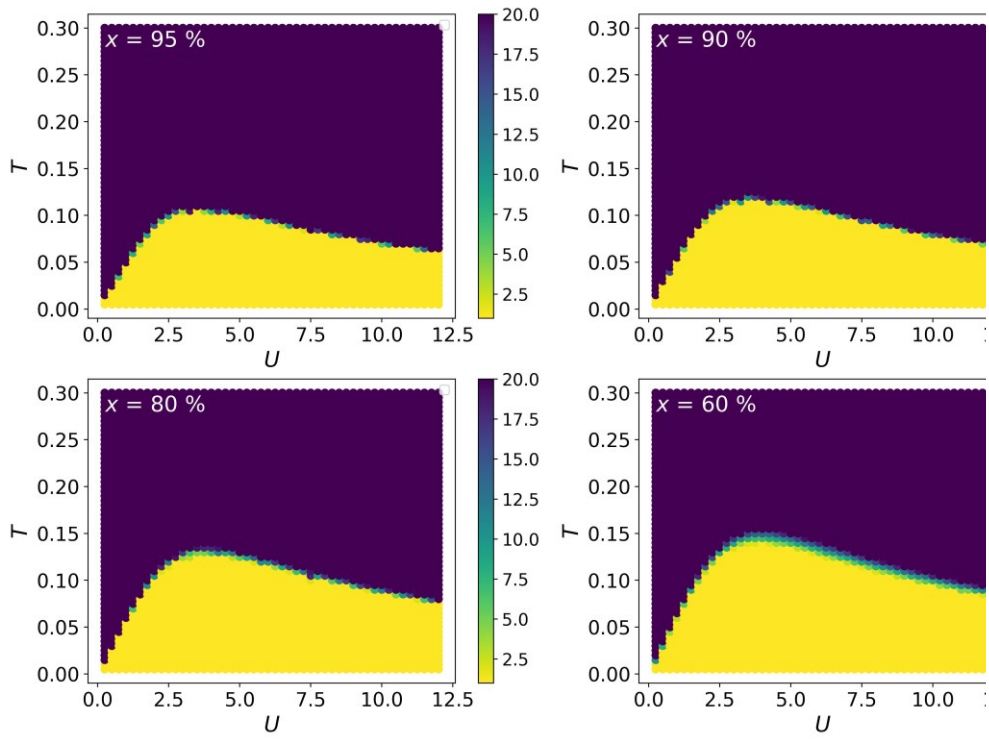

Fig. 7: The participation ratio for *d* electrons in L12 lattice. The percentage *x* of the described variance in the data is written in the upper left corner of each graph.

From both figures, it is clear that two different phases exist in our data. In the lower part of our graphs (yellow in color), only a few first explained variance ratio components describe most of the variance in data. This suggests that the data has some well-defined structure, i.e., most configurations are alike. This is true for the ordered phase where a checkerboard pattern of *f*-electrons is expected.

On the contrary, for the data in the upper dark blue part of our graphs, not even the first 20 explained variance ratio components are enough to describe its variance. (And possibly many more components would be needed, but only the first 20 were computed during our analysis, as having more of them would be of a little additional benefit). This indicates that the data in this part of the phase diagram is disordered.

Interestingly, the shape of the division in the graph exhibits a close resemblance to the shape of the phase boundary between the ordered and the disordered phase for the Falicov-Kimball model, which was shown in Fig. 1. And crucially, the behavior of these phases matches too. This means that principal component analysis can be used to distinguish the ordered and the disordered phase in the Falicov-Kimball model, although it is not yet clear where exactly their boundary should be, as the lower part of the graph gets bigger as we decrease the percentage *x* of the variance we want to be described.

To proceed our analysis further, we created graphs of the dependence of only the first explained variance ratio on *U* and *T* for L12 lattice for both *f* and *d* electrons. This is a sensible thing to do, since the first explained variance ratio plays the role of the order parameter, as was already mentioned in the section about the PCA method. These graphs are shown in Fig. 8.

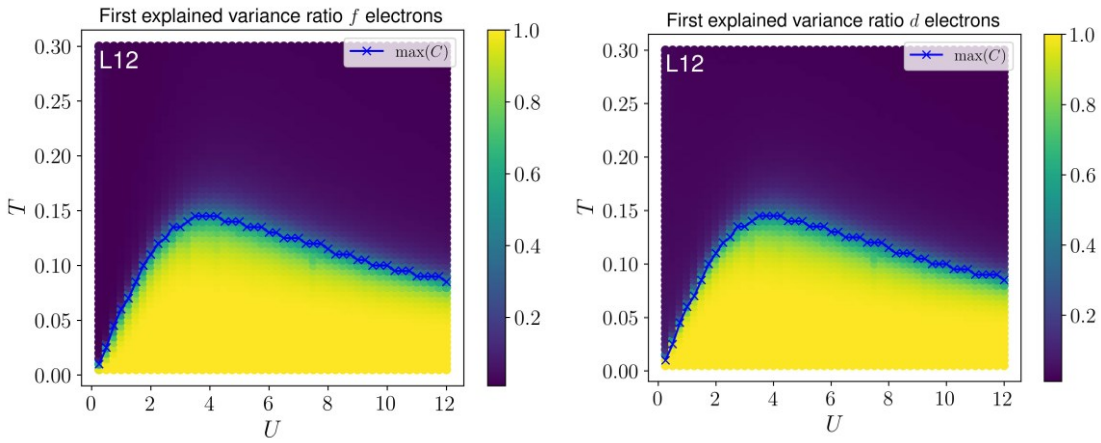

Fig. 8: The first explained variance ratio for L12 lattice for *f* electrons (left picture) and *d* electrons (right picture)

The blue line with x symbols in Fig. 8 represents positions of maxima of the specific heat from the MC simulation. This shows a different way to estimate critical points where the phase transition between the ordered and the disordered phase occurs.

Both graphs show a large value of the first explained variance ratio in the bottom yellow part. This means that the data for the corresponding U and T combinations is ordered because the order parameter is high and most of the variance in the data can be explained by the first explained variance ratio alone, which agrees with graphs of the participation ratio in Fig. 6 and Fig. 7. Unsurprisingly, the value of the first explained variance ratio is small in the upper dark blue part of the graph, where the data is disordered.

We further support the conclusions from graphs in Fig. 8 by showing a cut through these graphs for two different fixed values of potential U, namely $U = 4.0$ and $U = 8.0$ in Fig. 9. These graphs show the dependence of the first explained variance ratio on temperature only and for all lattice sizes (L6, L8 and L10, in addition to L12). Configurations of *d* electrons were used for these graphs, but graphs for *f* electrons look alike.

The first explained variance ratio is high for low temperatures, indicating an ordered structure, and then steeply falls down as the structure of the data becomes disordered. The point at about halfway through the fall of the curve signifies the presence of a critical temperature of the phase transition. Moreover, we can see that this temperature is a little bit different for the two fixed values of U (lower for $U = 8.0$), as is expected in accordance with the phase boundary between the ordered and the disordered phase from Fig. 8.

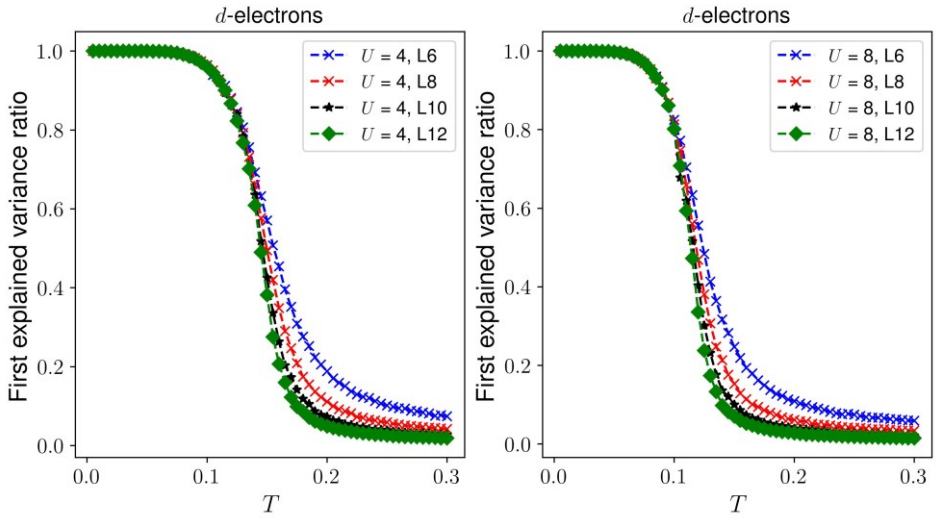

Fig. 9: Graphs of the dependence of the first explained variance ratio on temperature for fixed potential for *d* electrons. $U = 4.0$ for the left graph and $U = 8.0$ for the graph on the right.

Fig. 9 also illustrates, why mostly the L12 lattice will be used to present our results: Due to the finite size of all the lattices, the first explained variance ratio, which plays the role of the order parameter, does not fall sharply to zero at the critical temperature, but exhibits a continuous behavior instead. With larger lattice, this decline of the first explained variance ratio gets sharper, more closely approximating the ideal (but in practice unfeasible) case of the lattice of an infinite size.

Another way to confirm the correct identification of the critical temperature is presented in Fig. 10. There, for the same two fixed values of potential U as before ($U = 4.0$ and $U = 8.0$), the dependence of the normalized second explained variance ratio on temperature is shown, again for all lattices. The normalization was done by multiplying the second explained variance ratio by the number of sites in the lattice (144 for L12, 100 for L10, etc.). That way, all the curves in the graph should land on each other for sufficiently high temperatures. As before, *d* electrons were utilized to obtain these graphs, but graphs for *f* electrons look the same.

It was shown by Hu et al. that the second variation ratio can play a role of an effective susceptibility [25]. The susceptibility reaches its peak at the critical temperature of phase transition. However, we noticed that in our case the correct critical temperature more close matches the inflex point of the curve.

Therefore, the critical temperature can clearly be identified from both graphs in Fig. 10. Again, same as for Fig. 9, we can see that the critical temperature is lower for the graph with $U = 8.0$, which agrees with presence of the phase boundary between the ordered and the disordered phase from Fig. 8.

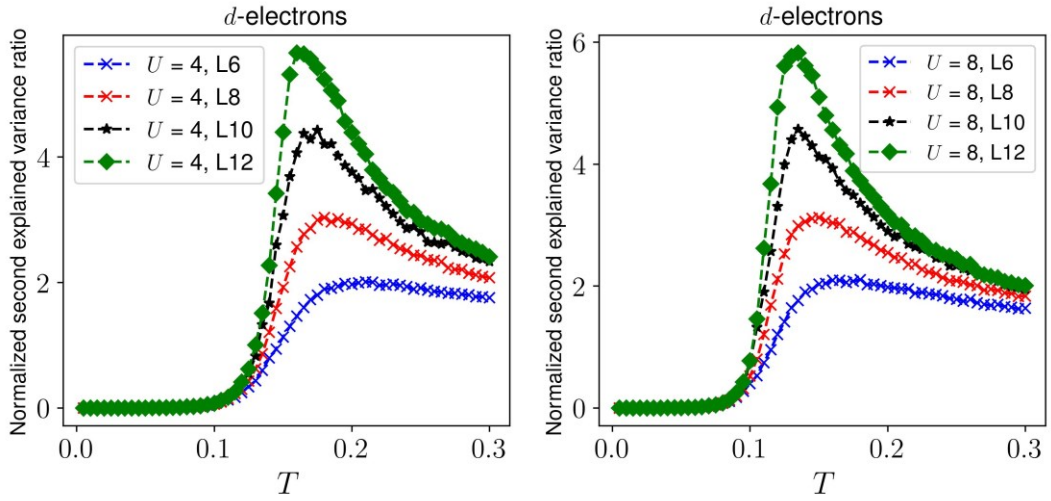

Fig. 10: Graphs of the dependence of the normalized second explained variance ratio on temperature for fixed potential for *d* electrons. $U = 4.0$ for the left graph and $U = 8.0$ for the graph on the right.

Finally, graphs of the second explained variance ratio dependence on U and T for L12 lattice were created for both *f* and *d* electrons, similar to the graphs of the first explained variance ratio in Fig. 8. These new graphs can be seen in Fig. 11.

The blue line symbols in Fig. 11 again represents positions of the maxima of the specific heat from the MC simulation, estimating critical points of where the phase transition between the ordered and the disordered phase occurs.

Both graphs in Fig. 11 show a small value of the second explained variance ratio for the ordered part, which is understandable, since most of the variance in the data is already accounted for by the first explained variance ratio, leaving little left to explain for the remaining explained variance ratios.

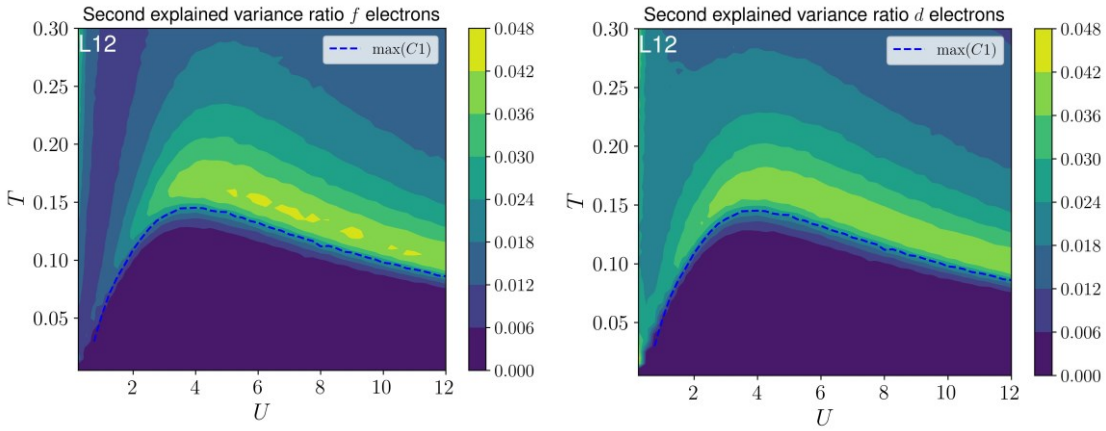

Fig. 11: The second explained variance ratio for L12 lattice for *f* electrons (left picture) and *d* electrons (right picture)

However, the second explained variance ratio is small for the disordered parts of the graphs as well, albeit bigger than for the ordered parts, as can be seen from the scale of the graphs, which shows that the second variance ratio does not explain more than 4,8 % of the data variance in vast majority cases. This also makes sense, since

the data in the rest of the graph is disordered and all the explained variance ratios are small for this type of data.

Although areas where the second explained variance ratio is slightly larger exist, there is no apparent boundary between different phases within the disordered part of the graph. Consequently, the second explained variance ratio, taken separately for *f* electrons and for *d* electrons, fails to provide information needed to discern the metal phase from the insulator one. But local differences within the disordered area still give us hope that some information needed to find the metal-insulator phase boundary may be present in the data.

3.1.2 PCA – Difference between explained variance ratios

Another attempt to find the phase transition boundary between different phases within the disordered part of the phase diagram using PCA was to subtract some explained variance ratio of *d* electrons from the same explained variance ratio of *f* electrons. The logic behind this approach was that the positions of *d* electrons with respect to *f* electrons provides information about the degree of correlation of the studied system. Therefore, it offers hope that we can find the phase transition between the DPs and DPw phases within the disordered phase using this information, because it can be expected that *f* and *d* correlation will be strong in the strong coupling regime and weak in the weak coupling regime. Luckily, this attempt proved to be successful.

Difference between first explained variance ratios for lattice L12 is shown in the left part of Fig. 12, while the difference between second explained variance ratios for the same lattice is shown in the right part of Fig. 12. Note that for the graph of second explained variance ratios, the scale of the colorbar was chosen in such a way that zero is in white color in the middle of the color range.

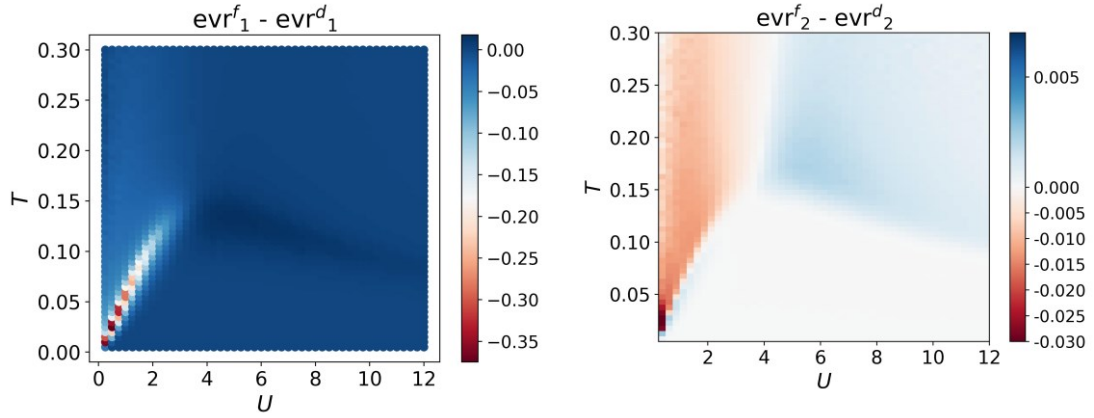

Fig. 12: Difference between first explained variance ratios of *f* electrons and *d* electrons (left). Difference between second explained variance ratios of *f* electrons and *d* electrons (right).

In the left graph, we can see in white the phase transition boundary between the ordered phase and the weakly localized phase from the disordered phase. This

phase transition is discontinuous, as was discussed in section about the Falicov-Kimball model.

In the same graph, the continuous phase transition boundary between the ordered phase and the rest of the disordered phase can also be seen in a darker shade of blue than its surroundings, although this boundary is not as clear as in prior graphs. Importantly, this graph shows that we can distinguish the type of phase transition (continuous vs. discontinuous).

In the right graph, the ordered phase is white in color, meaning that second explained variance ratios for *f* and *d* electrons are the same for this phase. Moreover, there is a difference between phases within the disordered phase. These phases are separated by a white stripe at approximately $U = 4.0$, where second explained variance ratios for *f* and *d* electrons are the same. The phase on the left has smaller second explained variance ratio for *f* electrons than for *d* electrons and is therefore red in the graph. The phase on the left is blue in the graph due to having bigger second explained variance ratio for *f* electrons than for *d* electrons.

The position of this boundary suggests that it is not a boundary between the metal phase and the insulator phase, but rather a boundary between the weakly localized phase and the Anderson insulator phase. This is an exciting discovery, since to our current knowledge, no ML based method was yet able to find a phase transition boundary between these two phases.

3.1.3 PCA Eigenpictures

To understand the character of ordering in different phases of the Falicov-Kimball model, it is useful to study the decomposition of electron configurations into their basis components. This is can be understood as an alternative to the structure factor. Therefore, in this section, we used the PCA method to create basis images (eigenpictures) of the electron configurations in our data, as was described in the corresponding Model and Methods subsection (2.4 PCA Eigenpictures). We never mixed *f* electrons configurations with *d* electrons configurations when creating eigenpictures. All eigenpictures shown in this section are created from L12 lattice configurations.

First, we created eigenpictures separately for some combinations of U and T. We chose U and T values in such a way that we covered the whole phase diagram, while having more eigenpictures towards lower U, where most changes between eigenpictures happen.

We chose potentials from $U = 0.5$ to $U = 10.5$ with step going from 0.5 at the beginning to 1.0 in the middle and to 2.0 at the end. Temperatures were chosen approximately uniformly from $T = 0.035$ to $T = 0.275$ with step 0.060.

In the following figures, we show how first and second eigenpictures change across the phase diagram both for *f* and for *d* electrons. First eigenpictures for *f* electrons are shown in Fig. 13, second eigenpictures for *f* electrons are depicted in Fig. 14. For *d* electrons, first and second eigenpictures for different U and T combinations are shown in Fig. 15 and Fig. 16 respectively.

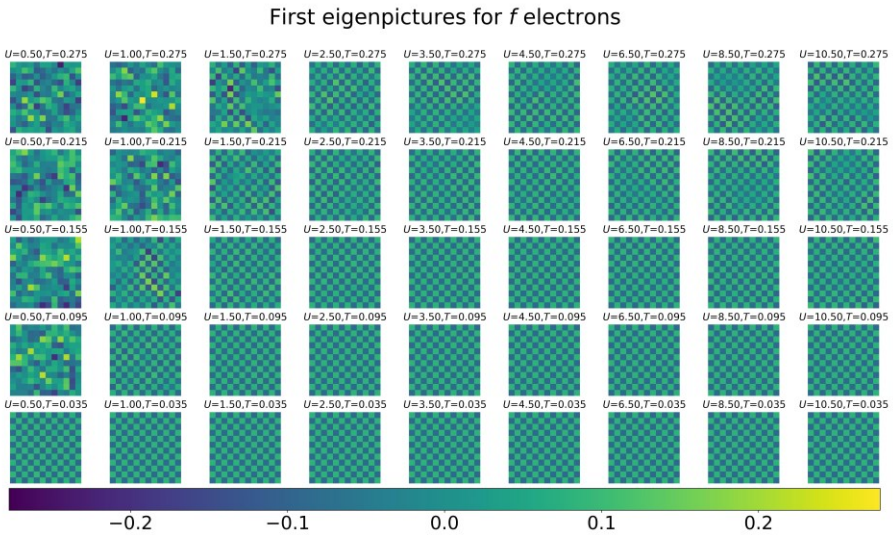

Fig. 13: First eigenpictures for *f* electrons for different combinations of *U* and *T* across the phase diagram. Temperature and potential values are written above each eigenpicture

From this figure, we can see that first eigenpictures for the ordered phase look like a checkerboard. The same can be said for the majority of first eigenpictures of the disordered phase, although parts of the checkerboard look sometimes a little "fuzzy". For low values of *U* and higher temperatures (see eigenpictures in the upper left part of the figure), no clear structure can be determined.

This agrees with our prior results when we calculated the participation ratio (see Fig. 6). There, we have shown that the data in the lower part of the phase diagram is ordered and almost everything is explained by the first component. Here we see the same thing as first eigenpictures (corresponding to the first component) are the checkerboard, which is the expected ordering of electron configurations in this part of the phase diagram, and therefore explain most of the variance in the data.

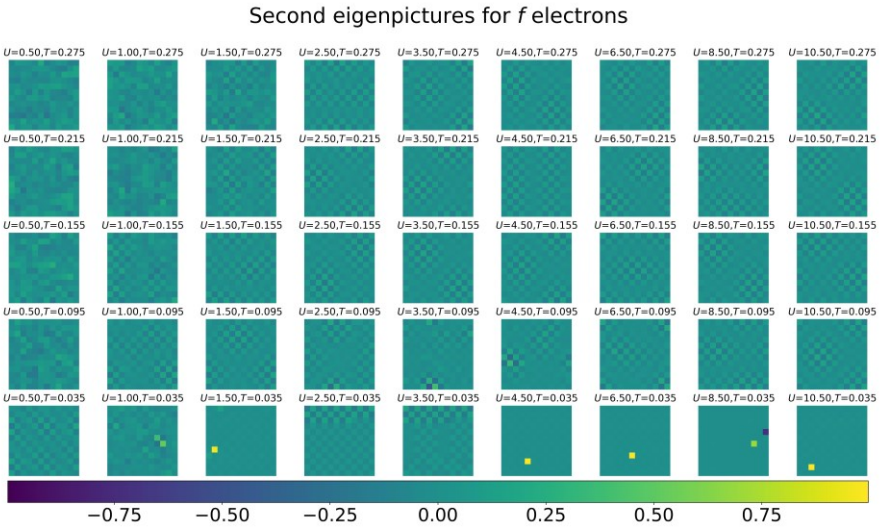

Fig. 14: Second eigenpictures for *f* electrons for different combinations of *U* and *T* across the phase diagram. Temperature and potential values are written above each eigenpicture

Second eigenpictures for low U and high T again show no obvious structure. For low T in ordered phase, second eigenpictures consist only of one or two small colored squares with rest of the picture having a uniform ocean color. This means that the electron configurations are highly ordered for these points of the phase diagram and second eigenpictures show a single or double site defects, which are deviations from the ordered checkerboard structure.

This again agrees with our prior results for the participation ratio (see Fig. 6). Since almost all variance was already explained by the first component, only a little to explain is left for the other components including the second one. Here, second eigenpictures represent only small deviation from the ordered checkerboard structure (see Fig. 14), which corresponds to the second component already explaining only a little.

The eigenpictures for the disordered phase and higher temperatures of the ordered phase consist of parts of the checkerboard and fuzzy parts between them. These eigenpictures resemble the ones that we would get if we used different fillings for Falicov-Kimball model [67] (as opposed to the half-filling used here), i.e. configurations which consist of checkerboard and homogeneous orderings. Because we have used grand canonical ensemble when generating our configurations, we can interpret our results like this: some eigenpictures resemble configurations from the half-filling and other encode configurations away from it.

This means that phases of the Falicov-Kimball model that are not half-filled can be seen in these eigenpictures, which in itself is exciting. However, there is no clear change in eigenpictures when going from the ordered to the disordered phase. Therefore, eigenpictures for f electrons do not enrich us with clear means of distinguishing phases of the half-filled Falicov-Kimball model.

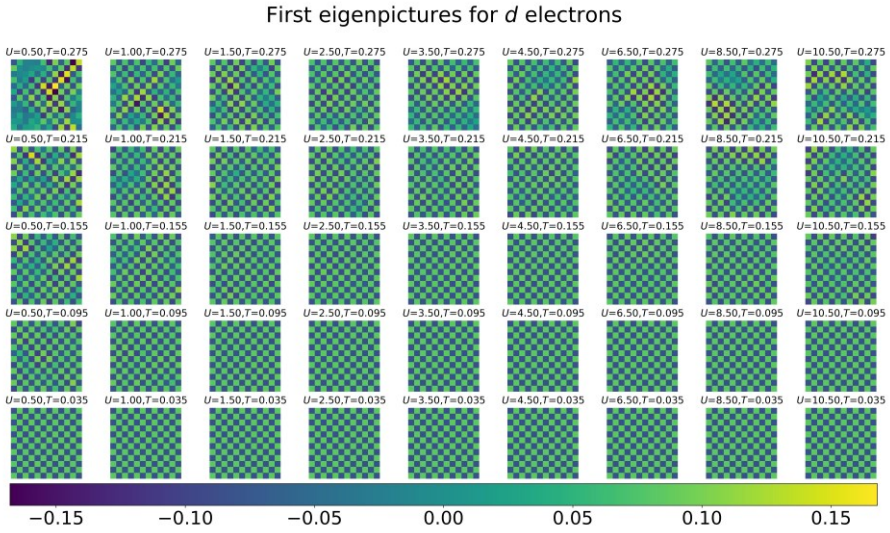

Fig. 15: First eigenpictures for d electrons for different combinations of U and T across the phase diagram. Temperature and potential values are written above each eigenpicture

First eigenpictures for *d* electrons look mostly the same as the first eigenpictures for *f* electrons (see Fig. 13). Only difference is visible for low *U* and high *T* eigenpictures, where a "fuzzy" checkerboard is present for *d* electrons, whereas no obvious structure was identifiable for *f* electrons.

Similarly, second eigenpictures for *d* electrons look mostly the same as the second eigenpictures for *f* electrons (see Fig. 14), with the only difference again being visible for low *U* and high *T* eigenpictures, where parts of checkerboard are present for *d* electrons, whereas no obvious structure was identifiable for *f* electrons. This means that *d* electrons are more ordered than *f* electrons for the upper left part of the phase diagram. Therefore, both the first and the second explained variance ratio for *d* electrons will be higher than for *f* electrons in this part of the phase diagram. This is in accordance with our findings from Fig. 12, where we showed difference between first and then second explained variance ratios of *f* and *d* electrons, which was negative (and therefore higher for *d* electrons).

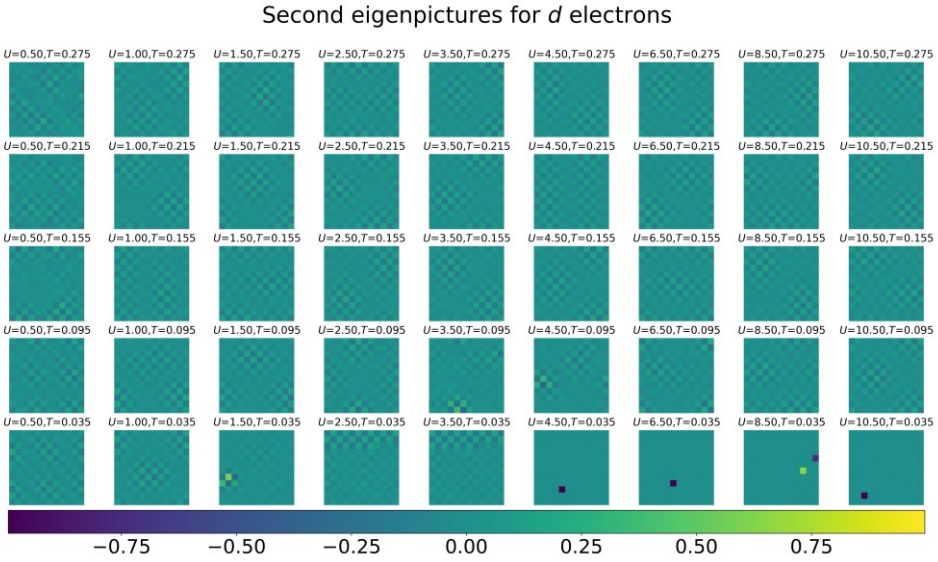

Fig. 16: Second eigenpictures for *d* electrons for different combinations of *U* and *T* across the phase diagram. Temperature and potential values are written above each eigenpicture

Also, similarly as for *f* electrons, eigenpictures for *d* electrons agree with prior results obtained for the participation ratio of *d* electrons (see Fig. 7).

However, there is still no clear change in eigenpictures when going from the ordered to the disordered phase. To better see the difference between eigenpictures of different phases, we chose some combinations of *U* and *T*, for which we show first 5 eigenpictures. These combinations of *U* and *T* were chosen in such a way that two were from the ordered phase (OP), one from the disordered phase for weak interaction (DPw) and one from the disordered phase for strong interaction (DPs). All these eigenpictures are shown in Fig. 17. Each set of eigenpictures is labelled with corresponding temperature and potential values, while information about the type of phase for given *U* and *T* is provided in the description of the figure. Because

eigenpictures for *f* and *d* electrons are mostly the same, we show only eigenpictures for *d* electrons here

The chosen temperatures and potentials were: $T = 0.045$, $U = 3.5$ and $T = 0.075$, $U = 8.5$ for ordered phase, $T = 0.235$, $U = 2.5$ for DPw phase and $T = 0.205$, $U = 11.5$ for DPs phase.

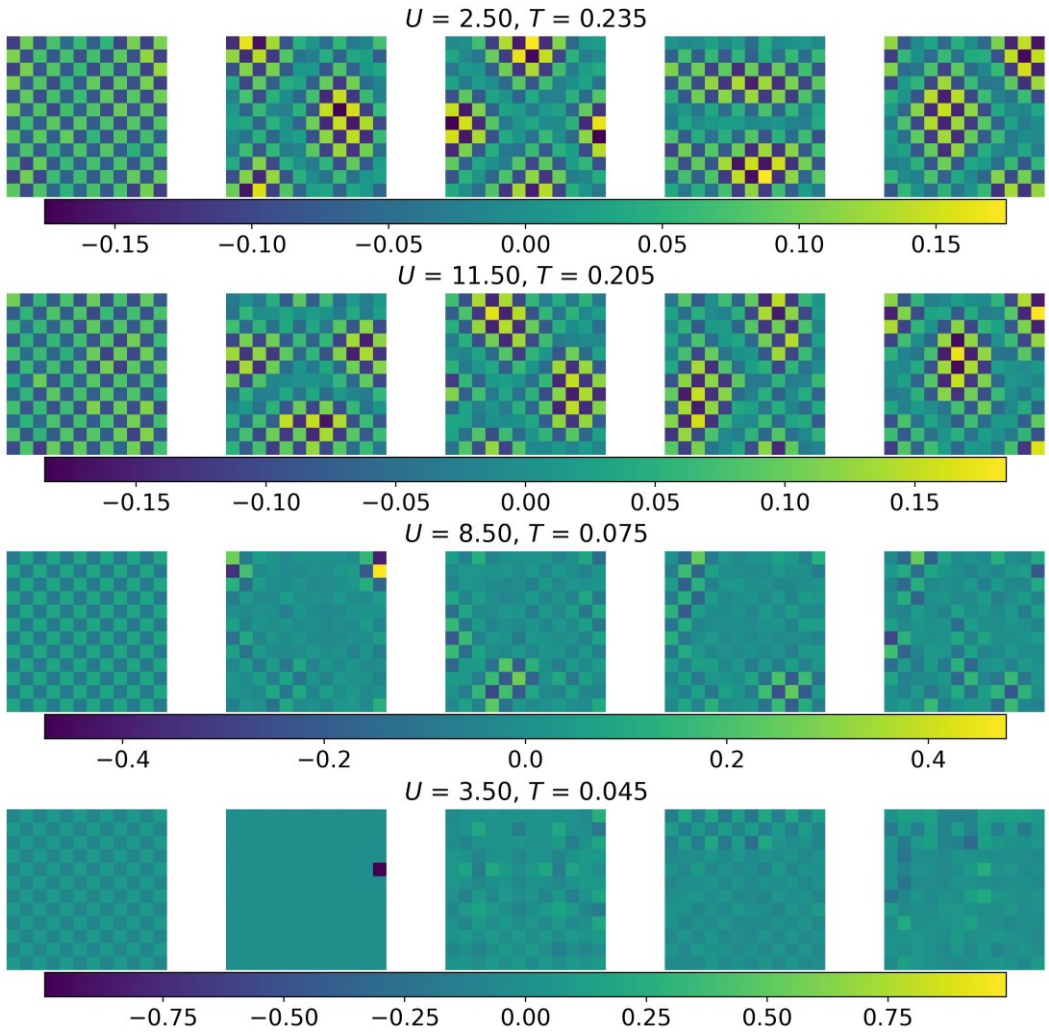

Fig. 17: First 5 eigenpictures for *d* electron configurations for 4 different U and T combinations. Last two combinations are for the ordered phase, first combination is for the DPw phase and the second combination is for the DPs phase.

We can clearly see that the last combination of U and T belong into the ordered phase, as only the first eigenpicture is a checkerboard and all the remaining eigenpictures have little to no structure.

However, for the third combination of U and T, the eigenpictures after the first eigenpicture have parts of checkerboard visible in them. Although these checkerboard parts are not as prominent as for the first two combinations of U and T that belong to the disordered phase, they suggest that a clear boundary between the ordered and the disordered phase cannot be found using the eigenpictures alone. Moreover, the figures show that as we increase the temperature, the electron configurations become more and more disordered even within the ordered phase.

Furthermore, Fig. 17 shows that eigenpictures across the disordered phase look alike. Consequently, we cannot distinguish different phases of the disordered phase using their eigenpictures.

Finally, we wanted to see how eigenpictures look, if we perform PCA on all our data. That is, we effectively created a global basis for all our configurations. Here we show first 5 eigenpictures for *d* electron configurations in Fig. 18 and first 5 eigenpictures for *f* electron configurations in Fig. 19. From both figures, we can clearly see that bases for *f* and *d* electrons are similar. This was expected from previous eigenpictures for local configurations, which were also mostly similar for both types of electrons.

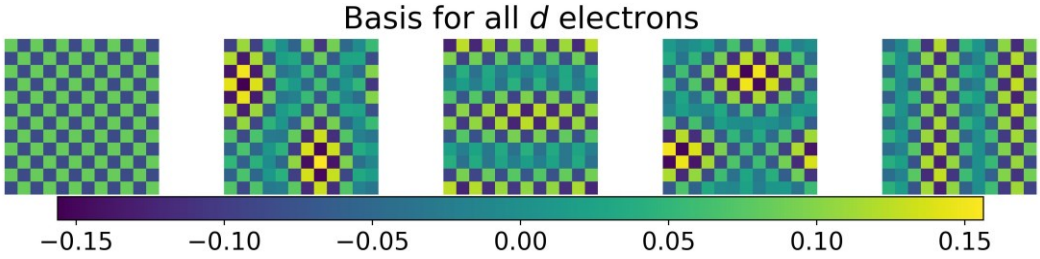

Fig. 18: First 5 eigenpictures for *d* electron configurations

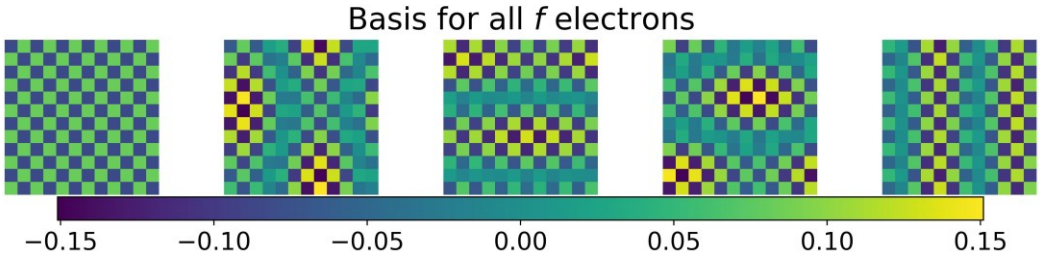

Fig. 19: First 5 eigenpictures for *f* electron configurations

From these figures, we see that the first component of the basis for all configurations is the checkerboard. The remaining four eigenpictures are parts of the checkerboard that corresponds to phases of Falicov-Kimball model outside of the half-filling [67].

3.2 Isometric feature mapping – Results

3.2.1 Simple Isometric feature mapping

Since the PCA method is a linear method, as was mentioned before, we have followed its mostly successful application by using some type of a non-linear method to reveal other patterns in our data that might have been missed by PCA.

The chosen approach in this study was isometric feature mapping (Isomap) [81] which was implemented using the sci-kit learn software [82]. The Isomap method was applied to our data in a similar fashion to the PCA method before and both to *f* electrons and *d* electrons as well. The only difference was that instead of calculating explained variance ratios as PCA does, Isomap calculated a reconstruction error. *The reconstruction error is the mean squared Euclidean*

distance between the data and reconstructed data and as such quantifies the loss of information [83].

A bitmap of the value of the reconstruction error for concrete values of potential U and temperature T was created. The bitmap for L12 lattice for f electrons is shown in Fig. 20.

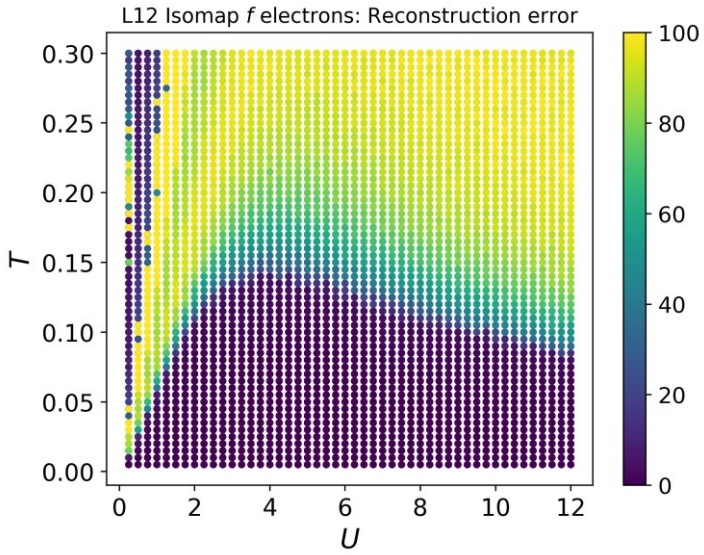

Fig. 20: The bitmap of the reconstruction error dependence on the temperature T and the potential U for f electrons for L12 lattice. The white area is caused by numerical instabilities.

Again, a clear distinction between the ordered and the disordered phase can be seen from Fig. 20. The ordered phase is dark blue in color this time, which corresponds to a low value of the reconstruction error. This means that the Isomap method has almost no trouble reconstructing the data, which suggests that its structure is regular and ordered, as it should be. The disordered phase is yellow in this figure, meaning higher value of the reconstruction error, which indicates that the data is disordered as the Isomap method has some trouble in reconstructing it.

However, no division is apparent within the disordered phase from these graphs for f electrons. That is why a similar bitmap was constructed for d electrons, which is shown in Fig. 21.

Here we can see that the reconstruction error for d electrons is not only low for the ordered phase, but also for the part of the disordered phase where the values of potential U are low. As a result, the distinction between the ordered and the disordered phase for low U values is unclear from this graph.

More importantly, two distinct phases can be seen within the disordered phase. However, the boundary between them is somewhat blurred as the reconstruction error changes continuously from low to high values. The reason for this very broad transition is not yet clear to us. However, we speculated that it is related to the transition from the weakly localized to the Anderson localized regime within the DPw phase described by Antipov et. al [5]. This would confirm our earlier findings from PCA approach, though the boundary between the two phases seems to be shifted here towards even lower U than $U = 4.0$ when doing PCA.

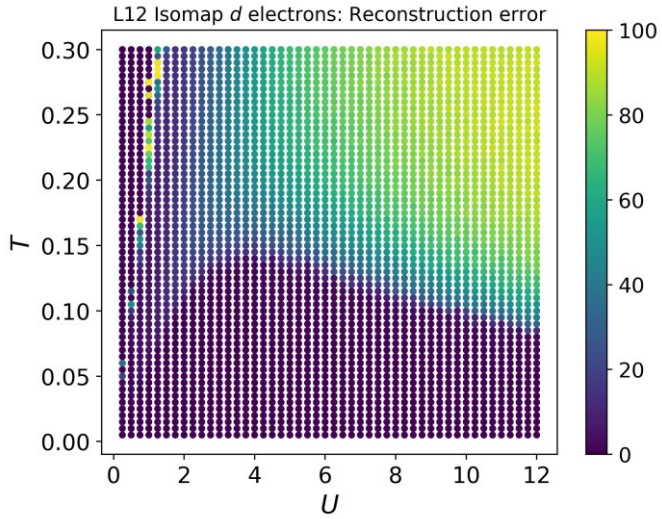

Fig. 21: The bitmap of the reconstruction error dependence on the temperature T and the potential U for d electrons for L12 lattice. The white area is caused by numerical instabilities.

To further confirm our findings, we combined the Isomap method with eigenenergies for particular configurations.

3.2.2 Isomap + Eigenenergies

Although the boundaries between the ordered and the disordered phase, and between the Anderson insulator phase and the weakly localized phase from the phase diagram of the Falicov-Kimball model from Fig. 1 were found, we have not yet found the boundary between the Anderson insulator phase and the Mott-like insulator phase. The information about this phase transition should be present in the single particle eigenenergies for particular configurations, because the Mott-like insulator phase has a finite gap in the density of states, which is not present in the density of states of the "metallic" phases.

Therefore, we investigate properties of the Falicov-Kimball model that are not available in experiment, but are accessible in MC simulation: The eigenenergies of electron configurations.

We diagonalized the Falicov-Kimball Hamiltonian (1) for fixed f electron configurations to get the diagonalized Hamiltonian (2) (see 2.2.1 Monte Carlo method for data generation subchapter) and obtained its eigenvalues. For each combination of U and T we calculated eigenvalues for each of the electron configurations and placed these eigenvalues into a new matrix. This meant that we had a 500 × 144 matrix for L12 lattice, because we had 500 configurations for each U and T and each hopping matrix had 144 eigenvalues.

We applied the Isomap algorithm to each of these matrices and calculated the reconstruction error, which is shown in Fig. 22. We have also added an expected position of the phase boundary between the Anderson insulator phase and the Mott-

like phase (as a yellow dashed line with points) to our graph. This boundary was created manually from the phase diagram of the Falicov-Kimball model (see the right part of Fig. 1), which was taken from the study by Antipov et al. [5].

Note that due to some outliers, for which reconstruction error was very high, we had to set the color bar limits manually to clearly see the difference between points in the disordered phase. We can observe that the reconstruction error is close to zero for the ordered phase and for the weakly localized part of the disordered phase. Whereas for the other parts of the disordered phase, reconstruction error is 5 or larger.

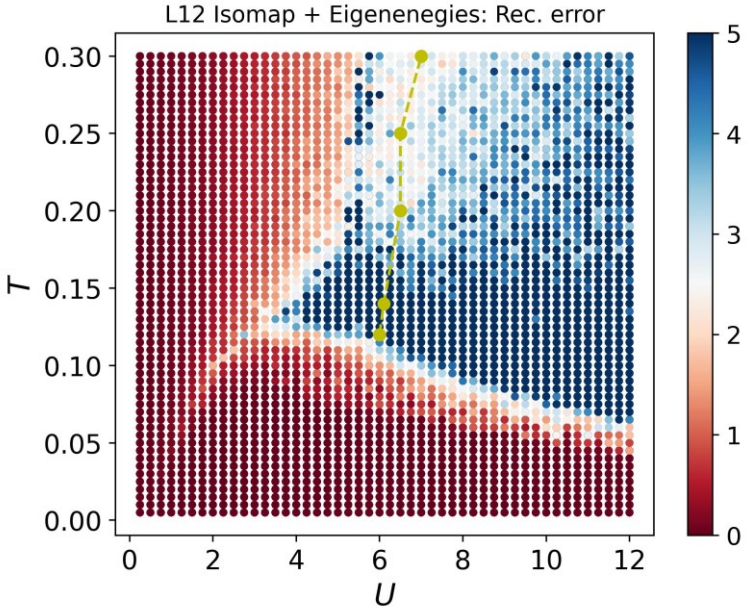

Fig. 22: The bitmap of the reconstruction error dependence on the temperature T and the potential U for eigenvalues calculated for L12 lattice configurations. The yellow dashed line with points shows an expected position of the phase boundary between the Anderson insulator phase and the Mott-like phase.
The points and the boundary are taken from the work of Antipov et. al [5]
(See Fig. 1 for full phase diagram from the aforementioned paper).

But it is worth mentioning that the reconstruction error within the disordered phase increases with increasing U and that the WL-AI boundary is not so clear. However, there are couple of points at about $U = 4.0$ and $U = 5.0$ where the reconstruction error is higher and it is likely that these points suggest a presence of the phase transition boundary.

More importantly, this method was not able to find the phase transition boundary between the Anderson insulator phase and the Mott-like insulator phase, as it seems that it found the WL-AI boundary instead. This can be also seen from the fact that the yellow dashed line with points representing the searched for boundary does not separate red and blue areas on the graph in Fig. 22.

In the next subchapter, we applied another ML technique, the prediction-base method, to further investigate presence of phase transition boundaries.

3.3 Prediction-based method – Results

After successfully applying both PCA and Isomap methods, we wanted to support our findings with another, preferably more elaborated method. The method we chose was the prediction-based method, primarily for its ability to identify phase boundaries, which was needed to aid in distinguishing the phases found within the disordered phase by our previous methods. As was described in the Predictors subchapter (2.7 Predictors), two different neural network types (Simple neural network, abbreviated SNN, and Modified SENet neural network) and one random forest regressor were used as predictors for this method. We first started with the Simple Neural Network.

3.3.1 Simple neural network (SNN)

3.3.1.1. *d* electrons

Because our previous results showed that *d* electron snapshots are more promising in distinguishing different phases within the disordered phase, we started with training our predictor on *d* electron configurations only.

To create a meaningful physical representation of our data for the neural network to train on, we had to modify the shape of our data a little bit. Therefore, for each combination of U and T, we took 16 random lines (configurations) from the corresponding file. Then we reshaped each of these lines into a square matrix, corresponding to the lattice, and stacked these matrices behind each other. To have multiple data points that would also be mostly independent, we repeated this process several times with other sets of random lines, which is also why only 16 out of 500 lines from each file were taken. Overall, we ended with approximately 100 different configurations for each U and T combination just for training the predictor, with different configurations being later used for evaluation. A different number of matrices could have been used, as a non-linear reader of this study might already know, however 16 seemed to be a good compromise between speed and precision.

When training our predictor, we trained it long enough so that the loss function of the validation data stopped changing significantly. However, to avoid overfitting, we stopped soon enough, so that the loss function of the validation data did not increase. A typical learning curve for the SNN can be seen in Fig. 23. Our testing showed that 20 epochs are enough for training the SNN.

Several different graphs were created for each lattice, but only the ones for L12 lattice will be shown here (as will be the case for all predictors used in the prediction-based method). Firstly, graphs showing the difference (in absolute value) between the temperature predicted by the SNN and the correct temperature at each given data point are shown in Fig. 24.

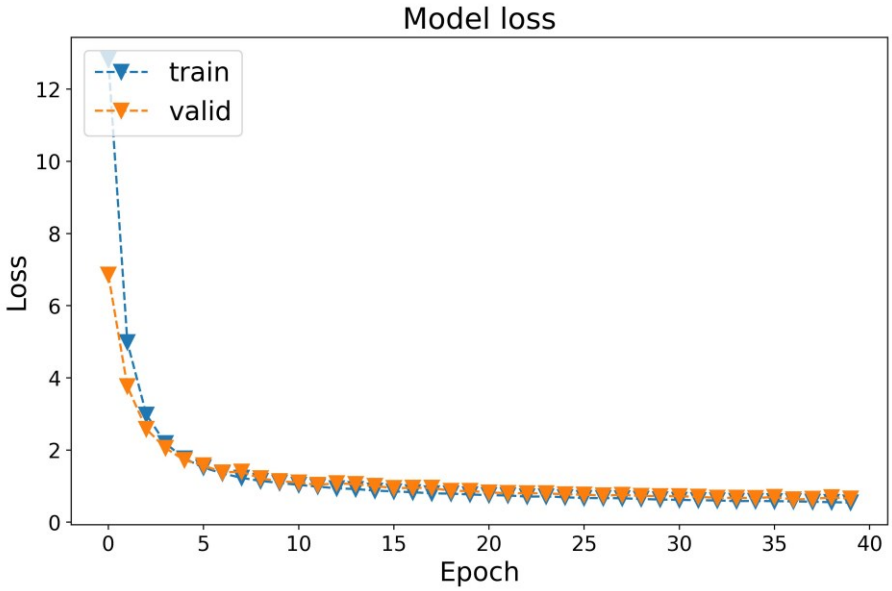

Fig. 23: Learning curve for the SNN for *d* electrons for L12 lattice. The blue triangles represent the loss function of the train data. The orange triangles represent the loss function of the validation data.

The left graph in Fig. 24 was created using the SNN that was trained on all temperatures. This graph shows that it is possible to distinguish the ordered and the disordered phase based on temperature. However, within both of these phases, the SNN is somewhat confused. A dark blue band across the whole graph within what should be the disordered phase is an example of this confusion. The explanation of this band is that the SNN cannot predict the temperature of different configurations within the disordered phase and so to minimize its loss, it predicts approximately the middle temperature from the disordered phase.

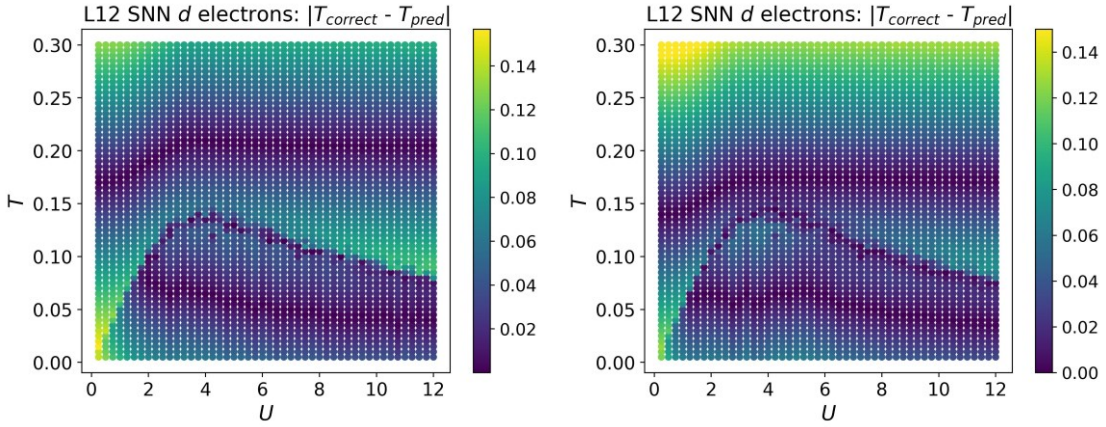

Fig. 24: Temperature predictions (by the SNN) for *d* electrons in L12 lattice. For the right image, only temperatures below 0.240 were used for training the predictor, whereas for the left image, all temperatures were used for training.

This explanation is supported by performing training of the SNN only on configurations with temperatures lower than 0.240. In that case, the dark blue band moves lower in accordance with the explanation, as is shown in the right image in

Fig. 24. A slightly darker blue area within the ordered phase in both graphs in Fig. 24 is likely an another example of the same phenomenon.

Similar graphs showing the difference (in absolute value) between the potential predicted by the SNN and the correct potential at each given data point are shown in Fig. 25.

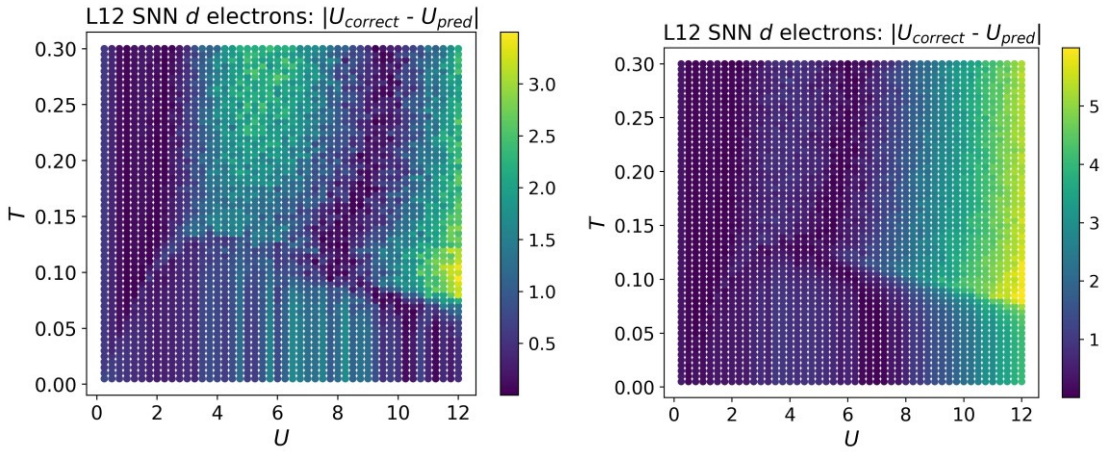

Fig. 25: Potential prediction for *d* electrons in L12 lattice. For the image on the right, only potentials below 8.0 were used for training the predictor, whereas for the left image, all potentials were used for training.

The left graph in Fig. 25 was made using the SNN that was trained on all potentials. Although a little bit unclear, a boundary between the ordered and the disordered phase can be seen in this graph. Moreover, in the upper left portion of the graph, the SNN finds it easier to predict the correct potential, which suggests a presence of distinct phase within the disordered phase, but the boundary of this phase again seems to be shifted to the left to lower U values than what is expected from the phase diagram for the Falicov-Kimball model from Fig. 1.

There is another part where the SNN is good at identifying the correct potential and that is a dark blue vertically oriented scimitar-shaped band in the disordered phase in the region approximately bounded by potential values of 7 and 10. The explanation of this band is the same as for the horizontal band in the case of temperature. This is proved by training the SNN only on potentials below 8.0, which leads to this band moving to the left as expected, which is shown in the right image in Fig. 25.

After that, a graph of the divergence of difference between the correct and predicted temperature with respect to temperature was created. Similarly, a graph of the divergence of difference between the correct and predicted potential with respect to potential was produced. Both these graphs are shown in Fig. 26.

For the temperature divergence, the phase boundary between the ordered and the disordered phase is clearly visible (in yellow). However, no such clear boundary exists when observing the potential divergence graph. The potential divergence is slightly higher where the WL-AI boundary could be, as well as where the boundary between the ordered and the disordered phase should be, especially for lower U

values. Unfortunately, none of these hints of phase boundaries could be considered significant.

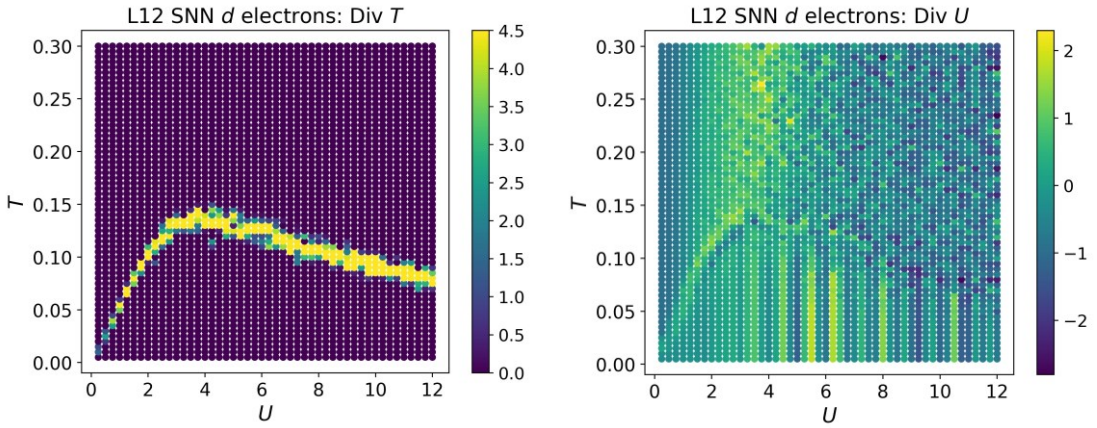

Fig. 26: Graphs of divergence with respect to temperature (left) and potential (right) for difference between the correct and predicted temperatures (left) and potentials (right) for *d* electron configurations in L12 lattice

Still, we would like to stress again that the method finds the phase transition boundary between the ordered and the disordered phase for all U values, which was not the case for the learning by confusion method [22].

3.3.1.2 *f* + *d* electrons

As our next step, we tried combining *f* electrons with *d* electrons, as it was unlikely that *f* electrons alone could fare any better than *d* electrons. Another argument for this approach was that it may be possible for the predictor to learn the strength of correlation between *f* and *d* electrons which could help in differentiating phases in the Falicov-Kimball model, as was the case for the PCA method when we subtracted explained variance ratios of *d* electrons from explained variance ratios of *f* electrons.

The input data for the predictor was prepared in a similar way as when using *d* electron alone. But to make our predictor even less computationally demanding, we used only two square matrices placed behind each other as an input, one for *f* electrons and the other for *d* electrons. (Multiple different number of matrices behind each other were tested, including up to 16 matrices, however all these attempts performed rather worse or equally at best compared to using two matrices only).

In the same way as for only *d* electrons before, graphs showing an absolute value of the difference between the correct and predicted values for both temperature and potential were created and are shown in Fig. 27.

The graph for temperature predictions is very similar to the one for *d* electrons only from Fig. 24. Therefore, temperature prediction is unlikely to offer any clues about distinct phases within the disordered phase.

The graph for potential predictions is in much darker shade of blue in the ordered phase. This means that the addition of *f* electrons into the mix helped the

predictor in predicting the correct potential for the configurations from the ordered phase.

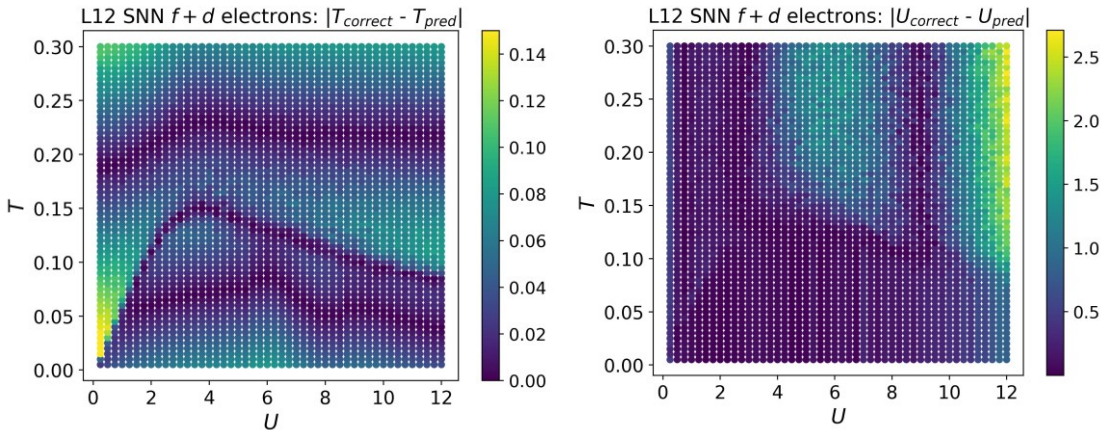

Fig. 27: Temperature (left) and potential (right) predictions (using the SNN) for $f + d$ electrons in L12 lattice

The upper left portion of the graph of potential predictions is also dark blue, same as in Fig. 25. This finding further supports the existence of a distinct phase in that area, which is likely to be the weakly localized phase from the phase diagram of the Falicov-Kimbal model in Fig. 1, judged by its position in the phase diagram.

Finally, the vertical blue band in the graph of potential predictions present around a potential of 9.5 is again caused by the fact that the predictor cannot distinguish different configurations within the right area of the disordered phase and predicts approximately a middle potential value from this area to minimize the loss function, as was already discussed before.

We also show here graphs of the mean-squared error for the difference between the correct and predicted values for both temperature and potential. These graphs are presented in Fig. 28.

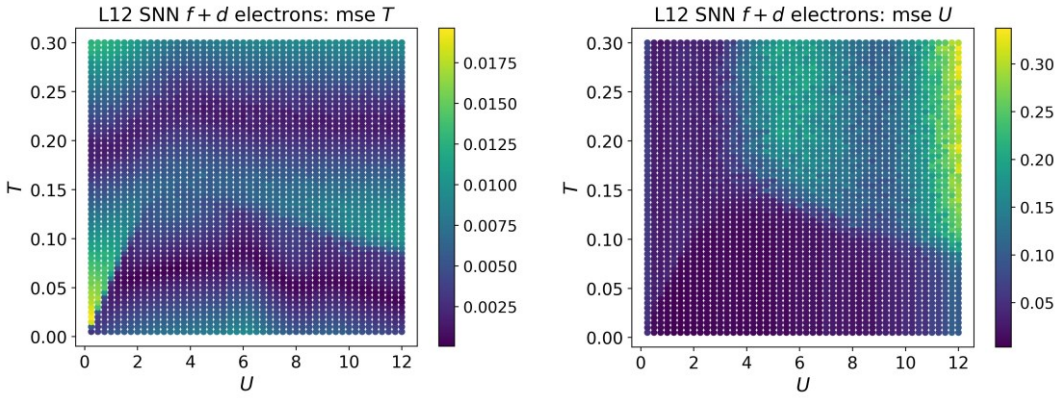

Fig. 28: The mean-squared error of the difference between the correct and predicted (by the SNN) values for temperature (left) and potential (right)

Graphs of the mean-squared error in Fig. 28 exhibits similar patterns as graphs of the difference between the correct and predicted values in Fig. 27, giving us yet another option of identifying phases in the Falicov-Kimball model.

To conclude this part of the study, in Fig. 29 we show graphs of divergence similar to the ones for d electrons only, but for $f + d$ electrons this time.

The temperature divergence shows the boundary between the ordered and the disordered phase in the same way as it already did for d electrons in Fig. 26. The potential divergence again hints at a possible presence of the WL-AI boundary within the disordered phase, as it did in Fig. 26 for d electrons only. However, still no clear boundary within the disordered phase exists as it does in the case of the ordered and the disordered phase when using divergence of temperature.

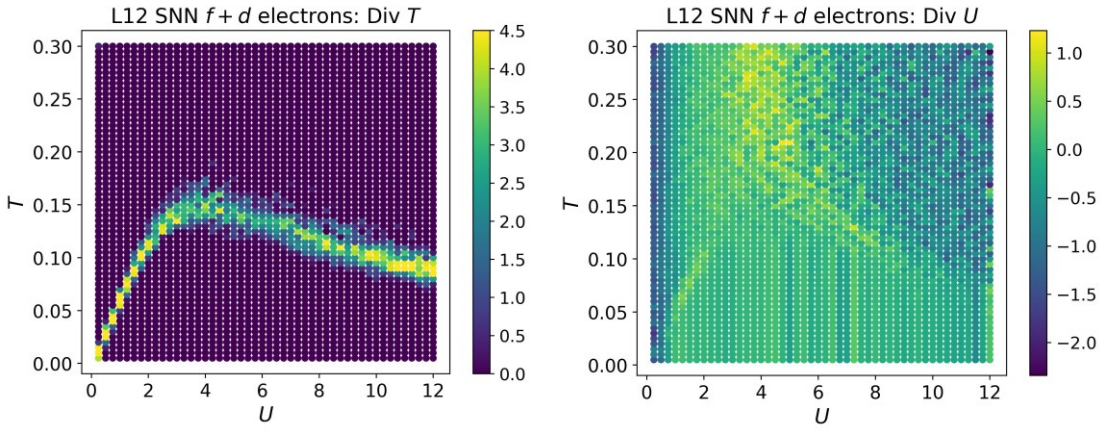

Fig. 29: Graphs of divergence with respect to temperature (left) and potential (right) for the difference between the correct and predicted (by the SNN) temperatures (left) and potentials (right) for $f + d$ electron configurations in L12 lattice

One additional type of graph was created for $f + d$ electrons and that is the graph of the divergence of the difference between the correct and predicted temperatures with respect to the potential U. This graph is shown in Fig. 30.

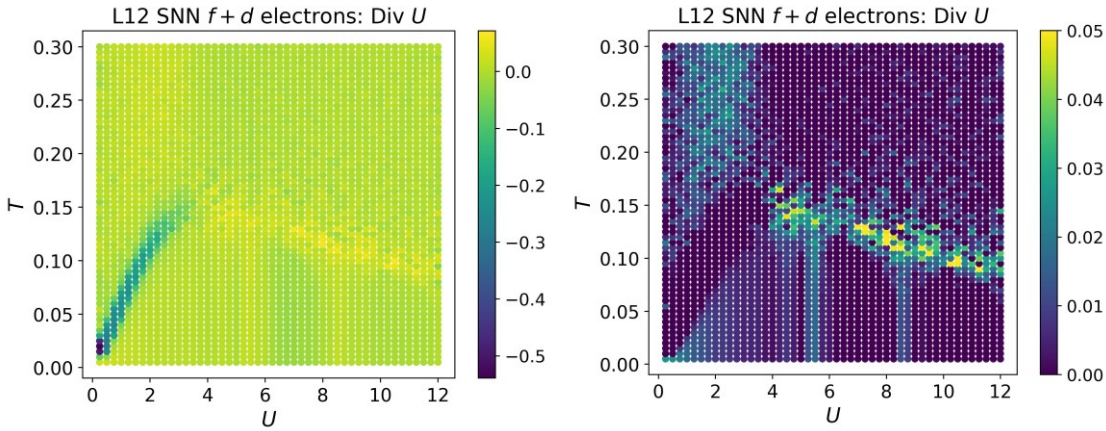

Fig. 30: Graph of the divergence with respect to potential for the difference between the correct and predicted temperatures (using the SNN) for $f + d$ electron configurations in L12 lattice. Two different scales are used for the same divergence values.

Two distinct phase boundaries can be seen in this graph, one clearly visible in blue, other less visible in bright yellow. To show the second phase boundary better, the same graph in a different scale is presented in the right part of Fig. 30.

These two distinct phase boundaries further support the idea that two distinct phases exist within the disordered phase, as each boundary likely correspond to a boundary between the ordered phase and a different part of the disordered phase. Crucially, their place in the graphs corresponds to when our previous analysis has shown these two phases to be, further supporting our results.

3.3.2 Modified SENet neural network

After applying the prediction-based method with the Simple neural network mostly successfully to the phase classification in the Falicov-Kimball model, we decided to confirm our results by using a different neural network as a predictor instead. We chose Squeeze-and-Excitation Network (SENet) [80], which is a publicly available neural networks that was already known to perform well on an image classification task, which bears many similarities to our problem due to the structure of our input data. We decided to use this particular neural network, because its architecture seemed to be best suited for our problem due to the presence of an SE block, as we have already explained in the Predictors subchapter (2.7 Predictors).

Due to the fact that the SENet network was suited for classifying images, which have the sizes of 256 × 256, we have to modify it by removing several convolution layers, as was already mentioned in the Predictors subchapter (2.7 Predictors). To avoid unnecessary large computational demand, we again stacked only two square matrices behind each other, one from f electron configurations and the other from d electron configurations. Also, only the results for $f + d$ electrons combination are shown here, because this combination yields better results than d electrons (or f electrons) alone, as was also the case for the prediction-based method with the SNN as its predictor.

To avoid overfitting, in a similar fashion to the SNN, we stopped soon enough during the training of the SENet network, so that the validation function did not increase. However, due to the large size of the Modified SENet network compared to the Simple neural network, each training epoch of the predictor took much more time, which led to less epochs needed to train the predictor. Usually, around 5 to 7 epochs were enough to satisfy our demands. An example of learning curve for the Modified SENet neural network can be seen in Fig. 31.

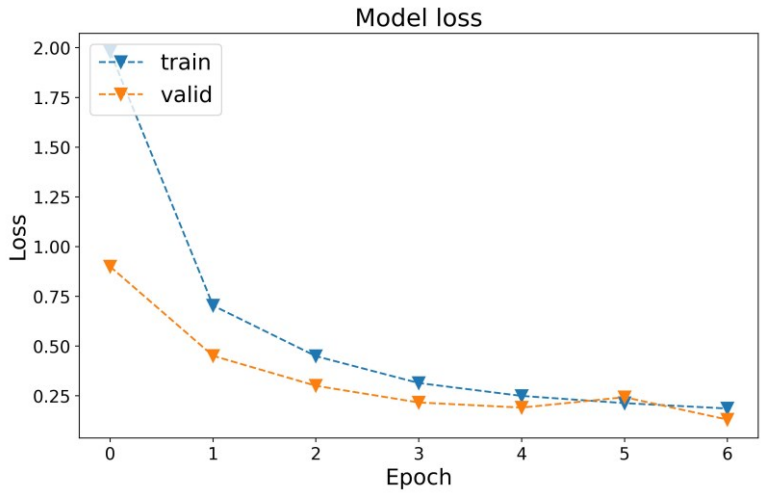

Fig. 31: Learning curve for the Modified SENet neural network for $f+d$ electrons for L12 lattice

The same graphs as for the Simple neural network were created using the Modified SENet network. The graphs showing an absolute value of the difference between the correct and predicted values for both temperature and potential are shown in Fig. 32.

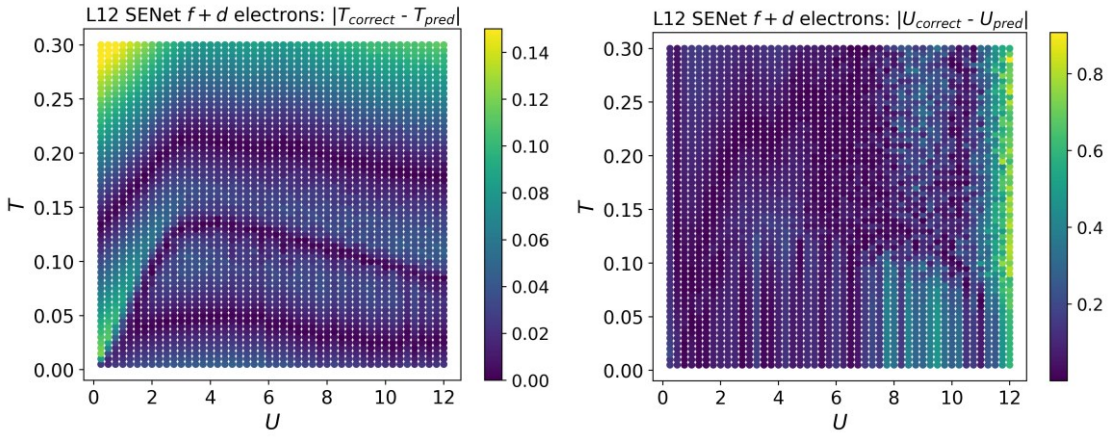

Fig. 32: Temperature (left) and potential (right) predictions (using the Modified SENet neural network) for $f+d$ electrons in configurations in L12 lattice

A similar pattern to the one found in Fig. 27 when using the SNN can be observed. This further aids in confirming that the results using the Simple neural network were correct. However, potential predictions are much better using the Modified SENet network, especially within the area of the disordered phase. This, ironically, does not help our case, as the difference between phases within the disordered phase is no longer apparent from the graph of potential predictions.

Graphs of the mean-squared errors also exhibit a similar pattern to their counterparts from Fig. 28 using the SNN, as is evident from Fig. 33. However, there is no evidence for the WL-AI boundary within the disordered phase in these graphs, which was somewhat hinted at in the graph of mean-squared error of potential when using the Simple neural network.

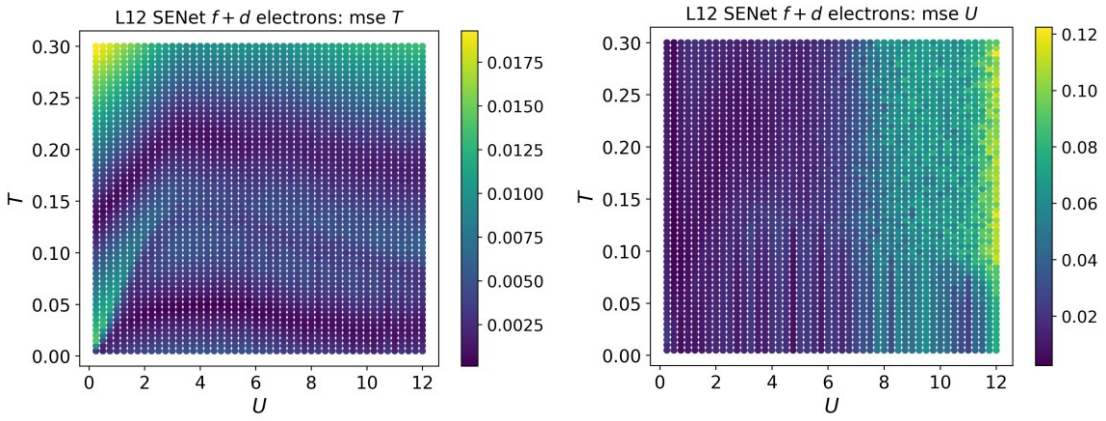

Fig. 33: The mean-squared error of the difference between the correct and predicted (by the Modified SENet neural network) values for temperature (left) and potential (right)

Finally, the graphs of divergence are shown in Fig. 34 and Fig. 35.

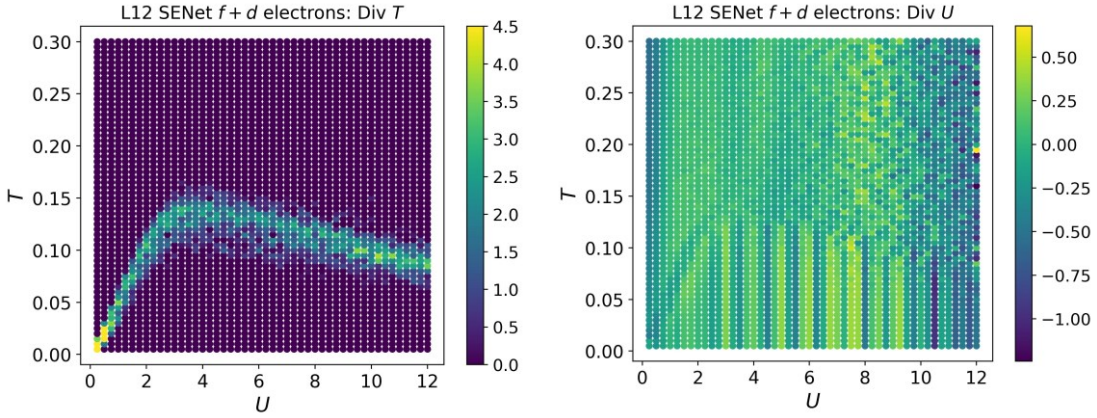

Fig. 34: Graphs of divergence with respect to temperature (left) and potential (right) for the difference between the correct and predicted (by the Modified SENet neural network) temperatures (left) and potentials (right) for $f + d$ electron configurations in L12 lattice

The phase boundary between the ordered and the disordered phase is clearly visible from the graph of temperature divergence in Fig. 34, although it is less prominent than when using the Simple neural network. The graph of the divergence of the potential in Fig. 34 offers little to no clues about any phase boundary.

Two distinct phase boundaries are again visible in the graph of the temperature divergence with respect to potential in Fig. 35. However, the boundary between the ordered phase and what is supposed to be the insulator phase is much less visible and may not be considered significant at all. Therefore, the same graph in different scale is shown in the right part of Fig. 35 to make this boundary somewhat visible.

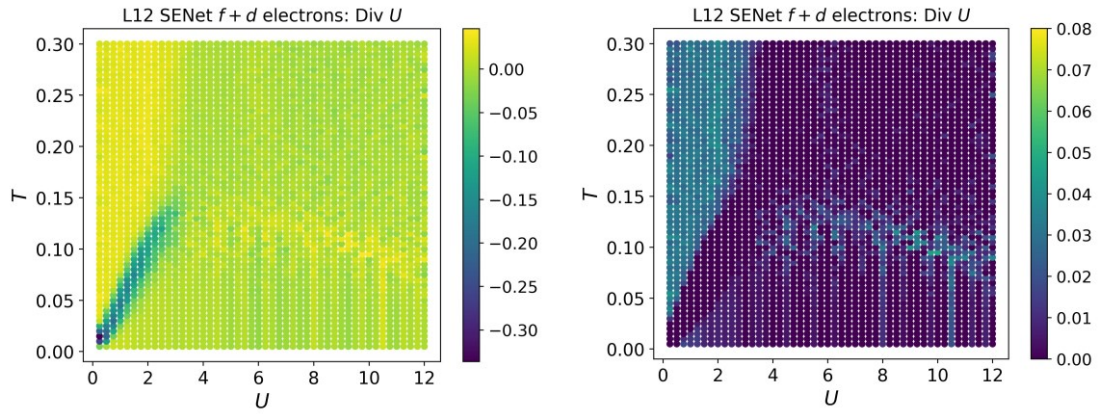

Fig. 35: Graph of divergence with respect to potential for the difference between the correct and predicted temperatures using the Modified SENet neural network for $f + d$ electron configurations in L12 lattice. Two different scales are used for the same divergence values.

To summarize this section, we have shown that a larger neural network may not always be a better predictor, as the Modified SENet network performed worse than the Simple neural network beforehand.

It is also worth noting that during our study, the application of the Modified SENet neural network has not always led to desired results, which is not obvious from the graphs shown here, because we only show the instances when it worked. The network was not able to train itself every time, especially in predicting the correct temperature. This was probably due to a random initialization of weights for different neurons in the network, which may have caused the predictor to get stuck in some local minima of loss function.

3.3.3 Random Forest

Random Forest is relatively simple, yet one of the most powerful ML algorithms, as was already mentioned in 2.7.4 Random Forest subchapter. Therefore we wanted to test if applying this algorithm as a predictor for the prediction-based method may offer some insight for distinguishing phases in the Falicov-Kimball model.

We followed a similar path with our use of the random forest regressor, as with the Simple neural network in subchapter 3.3.1 Simple neural network (SNN). However, we added predictions using f electrons alone, to see how well this method compares to other methods used in this study.

It is also worth noting that the random forest algorithm is not capable of reading 3-dimensional data and we had to adjust structure of our data accordingly as a result. In practice it meant that we did not reshape our electron configurations into 2D matrices as was the case for neural networks. Rather we kept our configurations as lines. Combining more configurations for one U and T was done by adding these lines below each other into a 2D matrix.

We tested several number of lines to use for one data point in our data. It turned out that 4 randomly chosen lines were optimal for our predictor´s performance, i.e. the predictor was working well enough and did not run too long.

3.3.3.1 *f* electrons

We tested several random forest regression predictors with different parameters. We settled on the predictor that consisted of 20 different decision trees and for which no regularization was present.

Although none of our random forest predictors trained on *f* electrons only was able to predict values of potential U well, the prediction of temperature T was much better, which is shown by the left part of Fig. 36, where the absolute value of the difference between the correct and predicted temperatures for each point of the phase diagram is shown. As a result, performing divergence on the difference between the correct and predicted temperature values, as was done for neural networks, produced a phase transition boundary between the ordered and the disordered phase, which can be seen in the right part of Fig. 36.

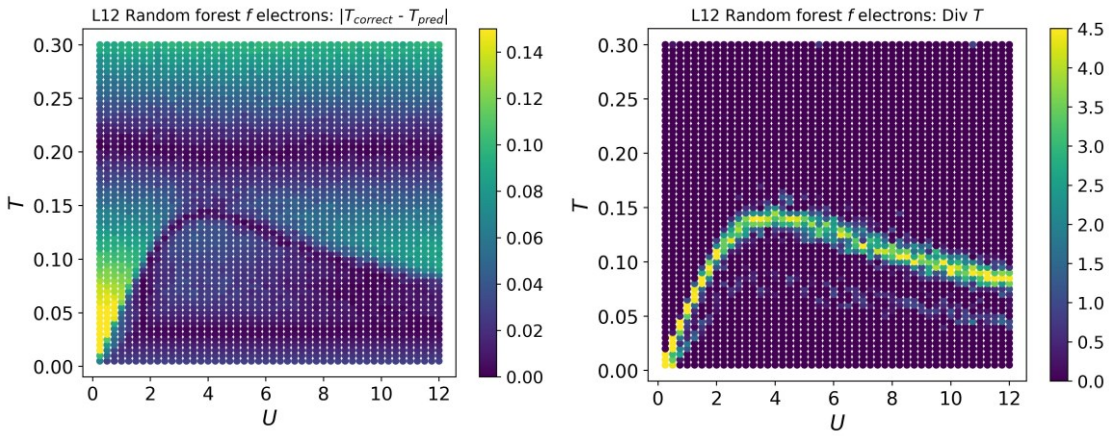

Fig. 36: Temperature predictions (left) and divergence with respect to temperature (right) for the difference between the correct and predicted (by the random forest regressor) temperatures for *f* electron configurations in L12 lattice.

3.3.3.2 *d* electrons

The same predictor used for *f* electron configurations was also applied to *d* electron configurations (after being trained on these configurations). Fortunately, this predictor worked much better for *d* electrons. Not only did the difference between the correct and predicted temperatures improved, as can be seen from the left part of Fig. 37, but the predictor was also capable of predicting potential values very well, which is shown in the right part of Fig. 37.

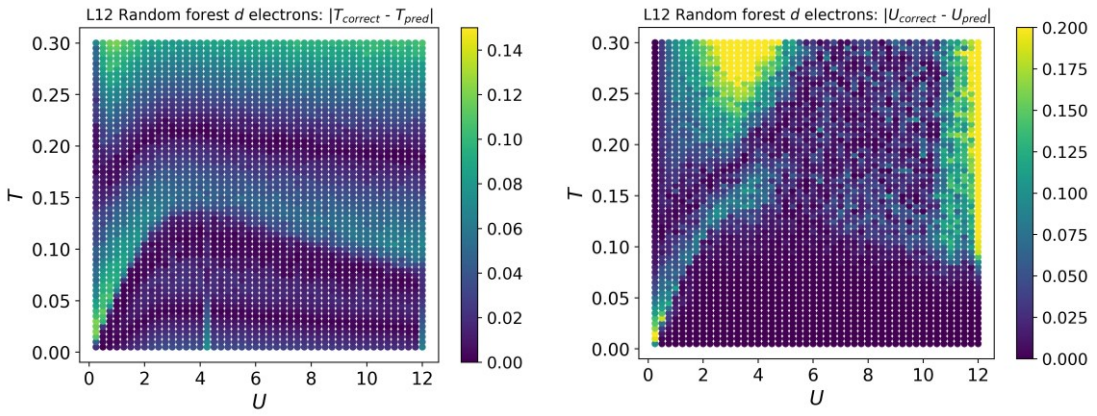

Fig. 37: Temperature (left) and potential (right) predictions (using the random forest regressor) for *d* electrons in configurations in L12 lattice

Consequently, the divergence of both temperature and potential showed promising results, though the divergence of potential offered only small hints about the phase transition boundary within the disordered phase. The graphs of both divergences are shown in Fig. 38.

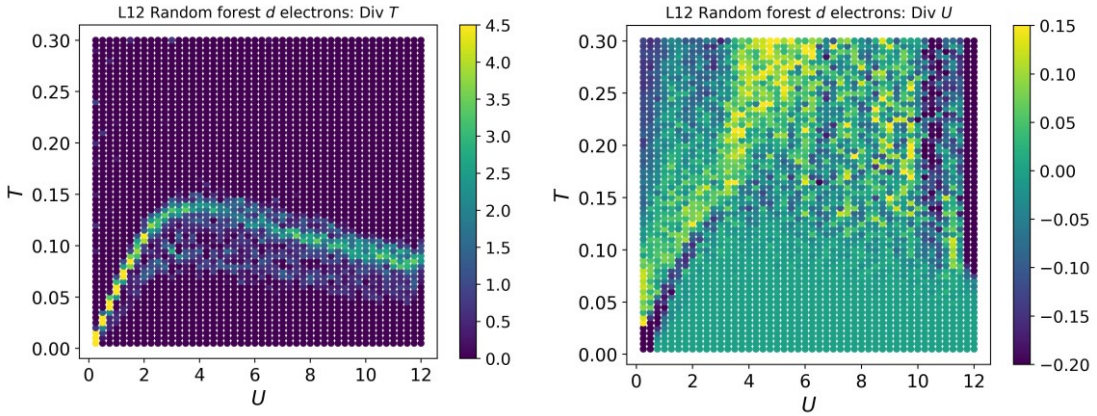

Fig. 38: Graphs of divergence with respect to temperature (left) and potential (right) for the difference between the correct and predicted (by the random forest regressor) temperatures (left) and potentials (right) for *d* electron configurations in L12 lattice

The left graph in Fig. 38 clearly shows the phase transition boundary (in yellow for lower U values and in light green for bigger U values) between the ordered and the disordered phase.

The right graph in Fig. 38 shows (in dark blue) the first part of the phase transition boundary between the ordered and the disordered phase, but only up until U values around 3. However, the ordered phase can still be identified from this graph thanks to the fact that the divergence is zero for all points within the disordered phase.

Some hints of the boundary within the disordered phase at values of U between 3 and 4 can also be seen in yellow in the potential divergence graph. The position of this boundary suggests that it should be the WL-AI boundary. However, this boundary is not very sharp and it is impossible to say if the higher divergence values were not caused by some artefacts in the random forest regressor.

Also note, that the color scale for the potential divergence graph had to be limited from below at -0.20 to actually see the hints of boundary. The reason for this modification of color scale was that due to us having data only for finite potentials the regressor´s predictions did not work well for the boundary values of potential (that is $U = 12.0$). As a result, the divergence for this value of potential was negative and very high in absolute value (almost -1). And in the correct scale, the possible phase transition boundaries are more difficult to see.

3.3.3.3 *f* + *d* electrons

Finally, we tried combining configurations for both *f* electrons and *d* electrons. We used the same random forest regressor as for separate *f* and *d* electrons before (trained on configurations of *f* + *d* electrons). The structure of our data points was also the same: We took four random lines (electron configurations) and placed them below each other. First and third of these lines were *f* electron configurations, while the other two were configurations of *d* electrons.

Predictions of both temperature and potential, shown in Fig. 39, seemed to be similar to the ones for *d* electrons alone. Unfortunately, divergences did not show any new insights, as is evident from Fig. 40.

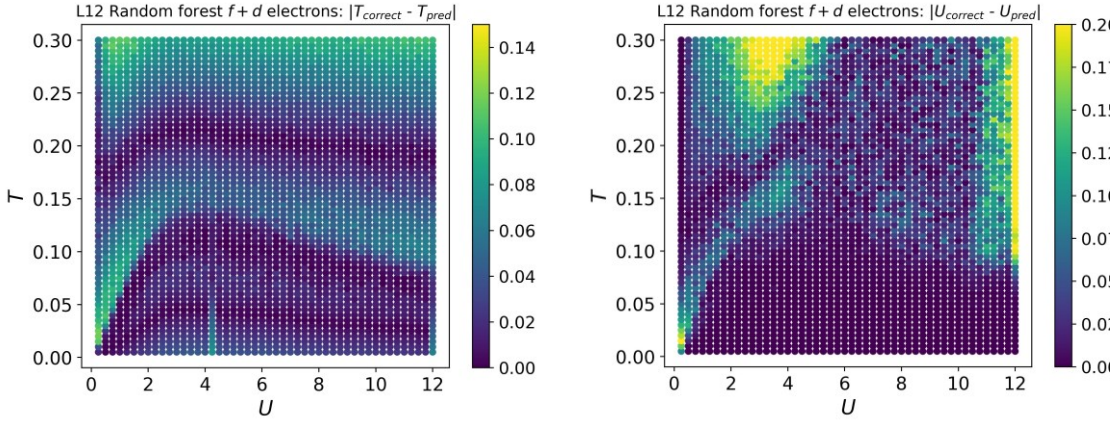

Fig. 39: Temperature (left) and potential (right) predictions (using the random forest regressor) for *f* + *d* electrons in configurations in L12 lattice

To summarize, the prediction-based was capable of reliably distinguishing the ordered phase from the disordered phase for all different predictors used (two neural networks and one random forest regressor). However, this method was not able to decisively distinguish different phases within the disordered phase.

To achieve that, we next tried combining the prediction-based method with the PCA method, because the latter one was able to find other phase transition boundaries.

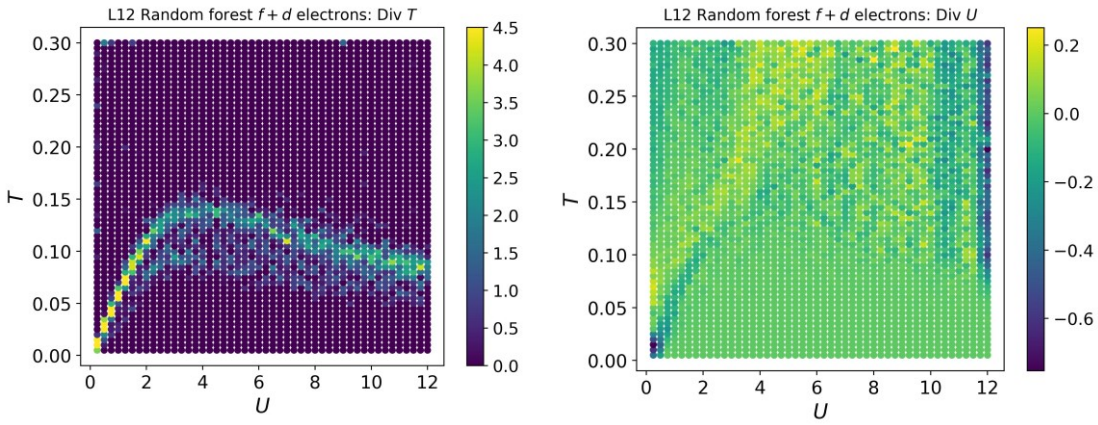

Fig. 40: Graphs of divergence with respect to temperature (left) and potential (right) for the difference between the correct and predicted (by the random forest regressor) temperatures (left) and potentials (right) for $f + d$ electron configurations in L12 lattice

3.3.4 Random Forest on PCA

The last method used in this study was a combination of two previously applied methods: PCA and random forest. First, PCA was applied to the data in the same way as before (see section 3.1) and first twenty explained variance ratios were calculated for both f and d electrons and for each combination of temperature T and potential U. The output of PCA was then used as the input for the random forest regressor.

The structure of input for the random forest for each T and U was: 20 explained variance ratios (evrs for short) of f electrons, followed by 20 evrs of d electrons, which were followed by the differences between the evrs of f and d electrons, multiplied by the size of the lattice L, which was either 10 or 12 based on the lattice used.

Due to having only one set of explained variance ratios for a given combination of U, T, electron type and lattice size L, it was necessary to use several lattice sizes in assessing the performance of our predictor. Because we needed the random forest regressor to make predictions for each input point from the phase diagram (that is for each combination of U and T) and we did not want to make predictions on points already included in training, we trained the random forest on data for one lattice size and made predictions on different lattice size. This turned out to work pretty well. The best results were obtained when using largest available lattice sizes. Therefore we train on data from lattice L12 and made predictions on data from lattice L10.

This strategy (training on smaller lattice calculated numerically and making predictions for larger lattice) can potentially be used for making predictions on real experimental data. It seems viable to train a predictor on smaller lattice and then apply it to much bigger real world lattice that was measured in an experiment, such as the cold atoms trapped in optical lattices [68].

We made similar graphs as those in subsections about random forest and Neural networks predictors. The graphs showing an absolute value of the difference

between the correct and predicted values for both temperature and potential are shown in Fig. 41.

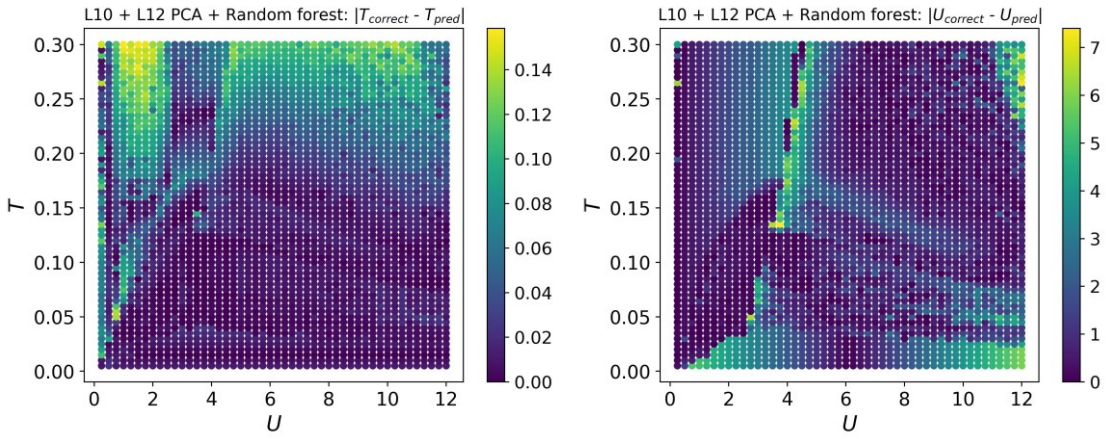

Fig. 41: Temperature (left) and potential (right) predictions on data from PCA using the random forest regressor trained on L10 lattice and making predictions on L12 lattice

For temperature, we can see that the predictor is able to make pretty accurate prediction in the ordered phase, but its predictions get less accurate with higher temperatures in the disordered phase. Moreover, there seems to be a difference in prediction accuracy for high temperatures in disordered phase at approximately $U = 4.0$, which suggests that there may be a boundary between two different phases. Although this in itself is not enough evidence for the existence of this boundary, it offers us hope that calculating the divergence of the difference might find the boundary.

Similarly, there is a clear line of decreased accuracy (in light green) for the right graph of potential predictions at approximately $U = 4.0$. This line even extends into the ordered phase, suggesting that maybe other aspects of the Falicov-Kimball model may be revealed when divergence will be performed on these predictions.

Fueled by hope from the predictions graphs, we created all four graphs of divergence - the divergence of both difference between the correct and predicted temperatures and the correct and predicted potentials with respect to both temperature and potential. However, since the graphs of divergence with respect to potential do not reveal any information about phase boundaries, they are not shown here. Graphs of the divergence with respect to temperature are present in Fig. 42.

Both graphs show us a boundary at approximately $U = 4.0$. For the divergence on temperature predictions, this boundary is in dark blue, whereas the divergence on potential predictions shows this boundary in light green. The place of this boundary suggests that it is the WL-AI boundary (see right phase diagram in Fig. 1), rather than the boundary between the metal and the insulator. This supports our findings from one of the PCA subsections, where we plotted the difference between explained variance ratios of *f* and *d* electrons, where we have also found this boundary.

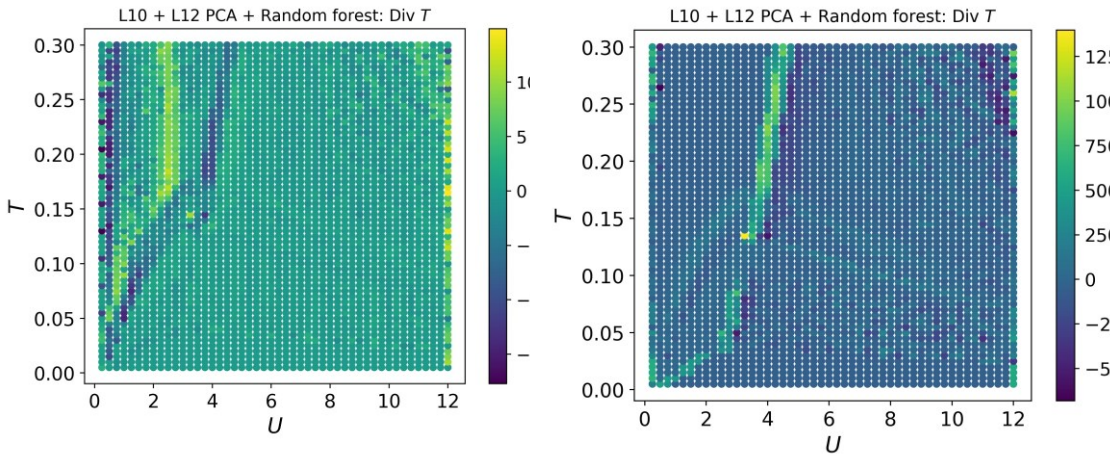

Fig. 42: Graphs of the divergence with respect to temperature for the difference between the correct and predicted temperatures (left) and for the difference between the correct and predicted potentials (right). Predictions are made on data from PCA using the random forest regressor trained on L10 lattice and making predictions on L12 lattice.

Moreover, hints of the boundary (again in blue) between the ordered phase and the weakly localized part of the disordered phase are present in the left graph. But this boundary was already found in this study using plethora of other methods

In the right graph, the light green line that is supposed to be a boundary between two types of disordered phase leaks into the ordered phase as well. This may suggest that it may be possible to distinguish some parts of the ordered phase, although it cannot be ruled out, that this extension of the line is just an artefact of the random forest regressor used for making predictions.

4. Discussion

The development of methods capable of distinguishing distinct phases in correlated electron systems without any prior knowledge is of great importance in condensed-matter physics. This study advanced this issue by demonstrating that the phase boundary between the ordered and the disordered phase in the Falicov-Kimball model is easily found, as virtually every method applied was capable of finding this boundary.

To our best knowledge, no one before has developed any unsupervised machine learning phase classification method capable of distinguishing the weakly localized and the Anderson insulator phase within the disordered phase of the Falicov-Kimball model. The results of this study indicate that this distinction is possible. Moreover, our findings suggest that the transition between the metal and the insulator might be more complicated than suggested by the presence or absence of a gap in the density of states (DOS) at the Fermi level, as mentioned in the 2.1 Falicov-Kimball model subchapter.

Our results support the existence of the two main phases in the Falicov-Kimball model: the ordered phase and the disordered phase. The fact that these phases were distinguishable using the principal component analysis method alone illustrates how powerful a tool this simple method can be. The Falicov-Kimball model is therefore another model, to which the PCA method can successfully be applied, adding to its previous application to the Ising, Blume-Capel, BSI and XY models [25].

Crucially, the PCA method was also capable of finding the WL-AI boundary, which was demonstrated in 3.1.2 PCA – Difference between explained variance ratios subchapter, where the difference between explained variance ratios for *f* electrons and for *d* electrons revealed this boundary.

The application of the isometric feature mapping (Isomap) proved to be another success of this study, as it was capable of distinguishing two different phases within the disordered phase. Moreover, this method, when applied to eigenenergies of electron configurations, was able to find a division between the weakly localized phase and the Anderson insulator phase in the Falicov-Kimball model, further supporting our findings from the application of the PCA method.

The prediction-based method was less successful in finding this division. Although hints at the presence of the WL-AI boundary were evident when using this method, the results are not conclusive. Therefore, further research is still needed to improve the prediction-based method in such a way that it will be able to precisely locate the WL-AI boundary using just raw Monte Carlo data or experimental snapshots. However, the application of this method is still deemed as a success, since, in contrast to other methods [22] it was capable of distinguishing the ordered and the disordered phase for all three different predictors used (two neural networks and one random forest regressor) in the whole range of U values.

Finally, application of the random forest regressor on data from PCA was also successful, as it again found the WL-AI boundary, and thus even more cementing

one of the main results of this study. Surprisingly, this method was not able to distinguish between the ordered and the disordered phase, but it did not matter to us, as this distinction was already achieved by every other method used in this study and was not main goal of applying the random forest regressor on PCA data.

It is important to acknowledge that lattices of a finite size were used in this study and that using larger lattices might provide additional information. We have shown that the boundary between the ordered and the disordered phase was becoming sharper by using larger lattice size. Therefore, it is possible that with even larger lattices, the WL-AI phase boundary could become sharper and hence more visible as well even for the prediction-based method.

Another limitation comes from the fact that our methods detect the presence of different phases, but does not interpret their behavior. Therefore, we may know that different phases exist, but not what their character is. Here the PCA method comes to rescue. This method can give us information about the orderliness of the phase, as we have shown. Furthermore, when creating eigenpictures of configurations using this method, we can actually see what the configurations of electrons look like in different parts of the phase diagram.

Although the prediction-based method performed great in finding phase transitions, it is not without its limitations. The main one comes from the fact that the predictor of the prediction-based method serves as a black box, which causes a lack of interpretability for some of the results.

Moreover, caution is needed when trying to make sense of the results, as we tried to illustrate (see Fig. 24 or Fig. 25) with areas in phase diagrams where predictors used in this method performed exceptionally well, even though nothing distinguished the data in these areas from the neighboring data. Therefore, some features in phase diagrams that had no scientific background may appear when using only the prediction part of this method. However, the main part of the method, the divergence, seem to be mostly unaffected by this problem. Still, some predictors were sometimes unable to find the desired features or found features that were not relevant to the given problem.

Furthermore, a predictor used in this method plays a significant role. Firstly, large enough resolution is needed for the method to work. With enough resolution, the main features are commonly found for all predictors. Such was the case for the phase boundary between the ordered and the disordered phase in this study. However, more hidden features may be difficult to find, as was the case for the WL-AI phase boundary.

We have also shown that a larger neural network may not always be a better predictor, as the Modified SENet network performed worse than the Simple neural network. It is worth noting that the application of the Modified SENet neural network has not always led to desired results. The network was not able to train itself every time, especially in predicting the correct temperature. This was probably due to a random initialization of weights for different neurons in the network, which may have caused the predictor to get stuck in some local minima of loss function.

5. Conclusion and outlook

The aim of this study was to perform an unsupervised phase classification of the Falicov-Kimball model using machine learning methods. Several different techniques were applied to this task, including principal component analysis (PCA), isometric feature mapping (Isomap) and the prediction-based method, for which two different neural networks and one random forest regressor were used as predictors. All these methods proved to be successful in distinguishing between the ordered and the disordered phase.

Moreover, all methods were able to reproduce the correct position of the boundary between these phases. Importantly, in contrast to previously applied learning by confusion, techniques used in this study worked reliably even for the first-order phase transition, which is the case for low values of potential U.

Crucially, the PCA method was capable of finding the boundary between the weakly localized phase and the Anderson insulator phase (the WL-AI boundary) within the disordered phase. This boundary was found by subtracting the second explained variance ratio of d electrons from the second explained variance ratio of f electrons

Furthermore, several other methods from this study supported the finding of the WL-AI boundary. Performing Isomap method on eigenenergies of electron configurations found this boundary. Random forest regressor applied to data from the PCA method also found the WL-AI boundary. And finally, some hints of this boundary were also present when using the prediction-based method with neural networks as its predictors.

The boundaries between the ordered and the disordered phase, and between the Anderson insulator phase and the weakly localized phase in the Falicov-Kimball model were found in this study by a plethora of techniques that were not applied before to this problem.

However, one of the main phase boundaries, the one between the Anderson insulator phase and the Mott-like insulator phase, from the phase diagram of the Falicov-Kimball model was not found. This is a problem for the future.

Outlook: Further possibilities remain as to how to find the remaining phase transition boundary in the phase diagram. For example, one of the unsupervised techniques that could be applied to this problem is an autoencoder. And even if the unsupervised methods fail, there still remains a possibility of using supervised learning for identifying the correct phases instead, although success in that case would be a bit less satisfying. All these options provide an excellent starting point for following studies. Moreover, it may also be helpful to test the methods on larger lattice sizes, however this is bound to be computationally more demanding.

Another interesting area of study may be the application of the Isomap method, which performed more than well in this study, to other model systems in condensed-matter physics. It is possible that hidden patterns in corresponding

structures may be revealed, leading to better understanding of phase diagrams of other models. Moreover, combining the Isomap method with eigenenergies of electron configurations worked surprisingly well. Therefore this technique is in our point of view also worth of further exploration.

Finally, since most of our methods performed well in finding phase transition boundaries in the phase diagram of the Falicov-Kimball model, the logical next step is to try applying these methods to other models, such as the t-J model, the Heisenberg model, the Hubbard model and their generalizations.

Overall, the study can be deemed successful, albeit great challenges still lie ahead.

Bibliography

[1] S. Paschen and Q. Si, "Quantum phases driven by strong correlations," *Nature Reviews Physics,* vol. 3, pp. 9-26, 2021.

[2] H. Čenčariková and P. Farkašovský, "Formation of charge and spin ordering in strongly correlated electron systems," *Condensed Matter Physics,* vol. 14, no. 4, pp. 1-66, 2011.

[3] A. Mazurenko, C. S. Chiu, G. Ji, M. F. Parsons, M. Kanász-Nagy, R. Schmidt, F. Grusdt, E. Demler, D. Greif and M. Greiner, "A cold-atom Fermi–Hubbard antiferromagnet," *Nature,* vol. 545, p. 462–466, 2017.

[4] R. Lemański and K. Ziegler, "Gapless metallic charge-density-wave phase driven by strong electron correlations," *Physical Review B,* vol. 89, no. 7, p. 075104, 2014.

[5] A. E. Antipov, Y. Javanmard, P. Ribeiro and S. Kirchner, "Interaction-Tuned Anderson versus Mott Localization," *Physical Review Letters,* vol. 117, no. 14, p. 146601, 2016.

[6] J. Arnold, F. Schäfer, M. Žonda and A. U. J. Lode, "Interpretable and unsupervised phase classification," *Physical Review Research,* vol. 3, no. 3, p. 033052, 2021.

[7] S. Sachdev, Quantum Phase Transitions, Cambridge: Cambridge University Press, 2011.

[8] N. Goldenfeld, Lectures On Phase Transitions and The Renormalization Group, 2018: CRC Press, Boca Ratton, FL.

[9] G. Carleo, I. Cirac, K. Cranmer, L. Daudet, M. Schuld, N. Tishby, L. Vogt-Maranto and a. L. Zdeborová, "Machine learning and the physical sciences," *REVIEWS OF MODERN PHYSICS,* vol. 91, no. 4, p. 045002, 2019.

[10] M. I. Jordan and T. M. Mitchell, "Machine learning: Trends, perspectives, and prospects," *Science,* vol. 349, no. 6245, p. 255, 2015.

[11] M. Pankaj, M. Bukov, C.-H. Wang, A. G. Day, C. Richardson, C. K. Fisher and D. J. Schwab, "A high-bias, low-variance introduction to Machine Learning for physicists," *Physics Reports,* vol. 810, pp. 1-124, 2019.

[12] U. Wolff, "Collective Monte Carlo Updating for Spin Systems," *PHYSICAL REVIEW LETTERS,* vol. 62, no. 4, p. 361, 1989.

[13] C. P. Robert, Monte Carlo Methods, Hoboken, New Jearsey: Wiley, 2004.

[14] H. G. Katzgraber, "Introduction to Monte Carlo Methods," *arXiv,* p. arXiv:0905.1629, 2011.

[15] J. Carrasquilla and R. G. Melko, "Machine learning phases of matter," *Nature Physics,* vol. 13, p. 431, 2017.

[16] L. Wang, "Discovering phase transitions with unsupervised learning," *PHYSICAL REVIEW B,* vol. 94, no. 19, p. 195105, 2016.

[17] E. P. L. v. Nieuwenburg, Y. H. Liu and S. D. Huber, "Learning phase transitions by confusion," *Nature Physics,* vol. 13, p. 435, 2017.

[18] P. Broecker, J. Carrasquilla, R. G. Melko and S. Trebst, "Machine learning quantum phases of matter beyond the fermion sign problem," *Scientific Reports,* vol. 7, p. 8823, 2017.

[19] K. Ch'ng, J. Carrasquilla, R. G. Melko and E. Khatami, "Machine Learning Phases of Strongly Correlated Fermions," *Physical Review X,* vol. 7, no. 3, p. 031038, 2017.

[20] S. J. Wetzel, "Unsupervised learning of phase transitions: From principal component analysis to variational autoencoders," *Physical Review E,* vol. 96, no. 2, p. 022140, 2017.

[21] J. Liu, Y. Qi, Z. Y. Meng and L. Fu, "Self-learning Monte Carlo method," *PHYSICAL REVIEW B,* vol. 95, no. 4, p. 041101, 2017.

[22] M. Richter-Laskowska, M. Kurpas and M. M. Maśka, "Learning by confusion approach to identification of discontinuous phase transitions," *Physical Review E,* vol. 108, no. 2, p. 024113, 2023.

[23] F. Schäfer and N. Lörch, "Vector field divergence of predictive model output as indication of phase transitions," *Physical Review E,* vol. 99, no. 6, p. 062107, 2019.

[24] E. Greplova, A. Valenti, G. Boschung, F. Schäfer, N. Lörch and S. D. Huber, "Unsupervised identification of topological phase transitions using predictive models," *New Journal of Physics,* vol. 22, p. 045003, 2020.

[25] W. Hu, R. R. P. Singh and R. T. Scalettar, "Discovering phases, phase transitions, and crossovers through unsupervised machine learning: A critical examination," *Physical Review E,* vol. 95, no. 6, p. 062122 , 2017.

[26] T. Kennedy and E. H. Lieb, "An itinerant electron model with crystalline or magnetic long range order," *Physica A (Amsterdam),* vol. 138, no. 1-2, pp. 320-358, 1986.

[27] J. Jędrzejewski, J. Lach and R. Łyżwa, "Ground state properties of the spinless Falicov-Kimball model: Crystallization and metal-insulator transitions off the hole-particle symmetry point," *Physica A (Amsterdam),* vol. 154, no. 3, pp. 529-543, 1989.

[28] C. Gruber, D. Ueltschi and J. Jędrzejewski, "Molecule formation and the Farey tree in the one-dimensional Falicov-Kimball model," *Journal of Statistical Physics,* vol. 76, p. 125–157, 1994.

[29] M. Plischke, "Coherent-Potential-Approximation Calculation on the Falicov-Kimball Model of the Metal-Insulator Transition," *PHYSICAL REVIEW LETTERS,* vol. 28, no. 6, p. 361, 1972.

[30] K. Michielsen, "Bond-charge–site-charge interaction and metal-insulator transitions," *PHYSICAL REVIEW B,* vol. 50, no. 7, p. 4283, 1994.

[31] A. Schiller, "Correlated hopping in the Falicov-Kimball model: A large-dimensions study," *PHYSICAL REVIEW B,* vol. 60, no. 23, p. 15660, 1999.

[32] M. H. Hettler, M. Mukherjee, M. Jarrell and H. R. Krishnamurthy, "Dynamical cluster approximation: Nonlocal dynamics of correlated electron systems," *PHYSICAL REVIEW B,* vol. 61, no. 19, p. 12739, 2000.

[33] T. Ribic, G. Rohringer and K. Held, "Nonlocal correlations and spectral properties of the Falicov-Kimball model," *PHYSICAL REVIEW B,* vol. 93, no. 19, p. 195105, 2016.

[34] T. Ribic, G. Rohringer and K. Held, "Local correlation functions of arbitrary order for the Falicov-Kimball model," *PHYSICAL REVIEW B,* vol. 95, no. 15, p. 155130, 2017.

[35] J. K. Freericks and V. Zlatić, "Exact dynamical mean-field theory of the

Falicov-Kimball model," *REVIEWS OF MODERN PHYSICS,* vol. 75, no. 4, p. 1333, 2003.

[36] J. K. Freericks, V. M. Turkowski and V. Zlatić, "Nonequilibrium Dynamical Mean-Field Theory," *PHYSICAL REVIEW LETTERS,* vol. 97, no. 26, p. 266408, 2006.

[37] H. Aoki, N. Tsuji, M. Eckstein, M. Kollar, T. Oka and P. Werner, "Nonequilibrium dynamical mean-field theory and its applications," *REVIEWS OF MODERN PHYSICS,* vol. 86, no. 2, p. 779 , 2014.

[38] T. Maier, M. Jarrell, T. Pruschke and M. H. Hettler, "Quantum cluster theories," *REVIEWS OF MODERN PHYSICS,* vol. 77, no. 3, p. 1027, 2005.

[39] V. Turkowski and J. K. Freericks, "Nonequilibrium perturbation theory of the spinless Falicov-Kimball model: Second-order truncated expansion in," *PHYSICAL REVIEW B,* vol. 75, no. 12, p. 125110, 2007.

[40] J. Kaye and D. Golež, "Low rank compression in the numerical solution of the nonequilibrium Dyson equation," *SciPost Physics,* vol. 10, p. 091, 2021.

[41] L. Huang and L. Wang, "Accelerated Monte Carlo simulations with restricted Boltzmann machines," *Physical Review B,* vol. 95, no. 3, p. 035105, 2017.

[42] M. M. Maśka and K. Czajka, "Thermodynamics of the two-dimensional Falicov-Kimball model: A classical Monte Carlo study," *PHYSICAL REVIEW B,* vol. 74, no. 3, p. 035109, 2006.

[43] M. Žonda, "Phase transitions in the Falicov–Kimball model away from half-filling," *Phase Transitions,* vol. 85, no. 1-2, pp. 96-105, 2012.

[44] V. Janiš, "A new construction of thermodynamic mean-field theories of itinerant fermions: application to the Falicov-Kimball model," *Zeitschrift für Physik B Condensed Matter ,* vol. 83, p. 227–235, 1991.

[45] S. Zhang, P. Zhang and G.-W. Chern, "Anomalous phase separation in a correlated electron system: Machine-learning–enabled large-scale kinetic Monte Carlo simulations," *PNAS,* vol. 119, no. 18, p. e2119957119, 2022.

[46] J. Arnold a F. Schäfer, „Replacing neural networks by optimal analytical predictors for the detection of phase transitions,“ *Physical Review X,* sv. 12, č. 3, p. 031044, 2022.

[47] M. Žonda, J. Okamoto and M. Thoss, "Gapless regime in the charge density wave phase of the finite dimensional Falicov-Kimball model," *Physical Review B,* vol. 100, no. 7, p. 075124, 2019.

[48] L. M. Falicov and J. C. Kimball, "Simple Model for Semiconductor-Metal Transitions: SmB6 and Transition-Metal Oxides," *PHYSICAL REVIEW LETTERS,* vol. 22, no. 19, p. 997, 1969.

[49] U. Brandt and C. Mielsch, "Thermodynamics and correlation functions of the Falicov-Kimball model in large dimensions," *Zeitschrift für Physik B Condensed Matter ,* vol. 75, p. 365–370 , 1989.

[50] U. Brandt and C. Mielsch, "Thermodynamics of the Falicov-Kimball model in large dimensions II," *Zeitschrift für Physik B Condensed Matter ,* vol. 79, p. 295–299, 1990.

[51] M. Žonda, P. Farkašovský and H. Čenčariková, "Phase transitions in the three-dimensional Falicov–Kimball model," *Solid State Communications,* vol. 149, no. 45-46, pp. 1997-2001, 2009.

[52] M. Gonçalves, P. Ribeiro, R. Mondaini and E. V. Castro, "Temperature-Driven Gapless Topological Insulator," *PHYSICAL REVIEW LETTERS,* vol. 122, no. 12, p. 126601, 2019.

[53] P. Haldar, M. S. Laad and S. R. Hassan, "Real-space cluster dynamical mean-field approach to the Falicov-Kimball model: An alloy-analogy approach," *PHYSICAL REVIEW B,* vol. 95, no. 12, p. 125116, 2017.

[54] V. Janiš and V. Pokorný, "Critical metal-insulator transition and divergence in a two-particle irreducible vertex in disordered and interacting electron systems," *PHYSICAL REVIEW B,* vol. 90, no. 4, p. 045143, 2014.

[55] U. Brandt and C. Mielsch, "Free energy of the Falicov-Kimball model in large dimensions," *Zeitschrift für Physik B Condensed Matter ,* vol. 82, p. 37–41, 1991.

[56] L. Chen, J. K. Freericks and B. A. Jones, "Charge-density-wave order parameter of the Falicov-Kimball model in infinite dimensions," *PHYSICAL REVIEW B,* vol. 68, no. 15, p. 153102, 2003.

[57] C. Gruber and N. Macris, "The Falicov-Kimball model: a review of exact results and extensions," *Helvetica Physica Acta,* vol. 69, pp. 850-907, 1996.

[58] R. Lemański, "Analysis of the Finite-Temperature Phase Diagram," *ACTA PHYSICA POLONICA A,* vol. 130, no. 2, p. 577, 2016.

[59] S. R. Hassan a H. R. Krishnamurthy, „Spectral properties in the charge-density-wave phase of the half-filled Falicov-Kimball model,“ *Phys. Rev. B,* sv. 76, č. 20, p. 205109, 2007.

[60] A. Kauch, P. Pudleiner, K. Astleithner, P. Thunström, T. Ribic and K. Held, "Generic Optical Excitations of Correlated Systems: π-tons," *PHYSICAL REVIEW LETTERS,* vol. 124, no. 4, p. 047401, 2020.

[61] P. Farkašovský, "Falicov-Kimball model and the problem of valence and metal-insulator transitions," *PHYSICAL REVIEW B,* vol. 51, no. 3, p. 1507, 1995.

[62] P. Farkašovský, "Pressure-induced insulator-metal transitions in the spinless Falicov-Kimball model," *PHYSICAL REVIEW B,* vol. 52, no. 8, p. R5463(R) , 1995.

[63] P. Haldar, M. S. Laad and S. R. Hassan, "Universal dielectric response across a continuous metal-insulator transition," *PHYSICAL REVIEW B,* vol. 99, no. 12, p. 125147, 2019.

[64] D. O. Maionchi, A. M. C. Souza, H. J. Herrmann and R. N. d. C. Filho, "Anderson localization on Falicov-Kimball model with next-nearest-neighbor hopping and long-range correlated disorder," *PHYSICAL REVIEW B,* vol. 77, no. 24, p. 245126, 2008.

[65] A. Smith, J. Knolle, D. Kovrizhin and R. Moessner, "Disorder-Free Localization," *PHYSICAL REVIEW LETTERS,* vol. 118, no. 26, p. 266601, 2017.

[66] R. Lemański, J. K. Freericks and G. Banach, "Stripe Phases in the Two-Dimensional Falicov-Kimball Model," *PHYSICAL REVIEW LETTERS,* vol. 89, no. 19, p. 196403, 2002.

[67] R. Lemański, J. K. Freericks and G. Banach, "Charge Stripes Due to Electron Correlations in the Two-Dimensional Spinless Falicov—Kimball Model," *Journal of Statistical Physics ,* vol. 116, p. 699–718, 2004.

[68] M. M. Maśka, R. Lemański, C. J. Williams and J. K. Freericks, "Momentum

distribution and ordering in mixtures of ultracold light- and heavy-fermion atoms," *Physical Review A,* vol. 83, no. 6, p. 063631, 2011.

[69] Y. Motome a N. Furukawa, „A Monte Carlo Method for Fermion Systems Coupled with Classical Degrees of Freedom," *J. Phys. Soc. Jpn.,* sv. 68, č. 12, pp. 3853-3858, 1999.

[70] J. Shlens, "A Tutorial on Principal Component Analysis," *arXiv,* p. arXiv:1404.1100, 2014.

[71] "Principal component analysis," Wikipedia, 12 August 2023. [Online]. Available: https://en.wikipedia.org/wiki/Principal_component_analysis. [Accessed 16 August 2023].

[72] L. Sirovich a K. Michael, „Low-dimensional procedure for the characterization of human faces," *Journal of the Optical Society of America A,* sv. 4, č. 3, pp. 519-524, 1987.

[73] Scikit-learn, "Faces dataset decompositions," 2007. [Online]. Available: https://scikit-learn.org/stable/auto_examples/decomposition/plot_faces_decomposition.html. [Accessed 21 March 2024].

[74] Scikit-learn, „The Olivetti faces dataset," 2007. [Online]. Available: https://scikit-learn.org/0.19/datasets/olivetti_faces.html.

[75] J. B. Tenenbaum, V. d. Silva and J. C. Langford, "A Global Geometric Framework for Nonlinear Dimensionality Reduction," *Science,* vol. 290, no. 5500, pp. 2319-2323, 2000.

[76] H. Murase and S. K. Nayar, "Visual learning and recognition of 3-d objects from appearance," *International Journal of Computer Vision,* vol. 14, pp. 5-24, 1995.

[77] J. W. McClurkin, L. M. Optican, B. J. Richmond and T. J. Gawne, "Concurrent processing and complexity of temporally encoded neuronal messages in visual perception," *Science,* vol. 253, p. 675, 1991.

[78] C. A. L. Bailer-Jones, M. Irwin and T. v. Hippel, "Automated classification of stellar spectra - II. Two-dimensional classification with neural networks and principal components analysis," *Monthly Notices of the Royal Astronomical Society,* vol. 298, no. 2, pp. 361-377, 1997.

[79] A. Géron, Hands-On Machine Learning with Scikit-Learn, Keras, and TensorFlow, 3rd ed., Sebastopol, CA 95472: O'Reilly Media, 2023.

[80] J. Hu, L. Shen, S. Albanie, G. Sun and E. Wu, "Squeeze-and-Excitation Networks," *arXiv,* p. arXiv:1709.01507, 2017.

[81] "2.2. Manifold learning," Scikit-learn, [Online]. Available: https://scikit-learn.org/stable/modules/manifold.html. [Accessed 16 August 2023].

[82] F. Pedregosa and e. al, "Scikit-learn: Machine Learning in Python," *Journal of Machine Learning Research,* vol. 12, pp. 2825-2830, 2011.

[83] "Dimensionality Reduction," Wolfram, [Online]. Available: https://www.wolfram.com/language/introduction-machine-learning/dimensionality-reduction/. [Accessed 16 August 2023].

[84] R. T. Scalettar, „An introduction to the Hubbard Hamiltonian," *quantum materials: experiments and theory,* sv. 6, 2016.

[85] A. M. Tonello, N. A. Letizia and D. R. a. F. Marcuzzi, "Machine Learning Tips

and Tricks for Power Line Communications," *IEEE Access,* vol. 7, pp. 82434-82452, 2019.

[86] K. M. Ang, E.-S. M. El-kenawy, A. A. Abdelhamid, A. Ibrahim, A. H. Alharbi, D. S. Khafaga, S. S. Tiang a W. H. Lim, „Optimal Design of Convolutional Neural Network Architectures Using Teaching–Learning-Based Optimization for Image Classification," *Symmetry,* sv. 14, č. 11, p. 2323, 2022.

[87] K. J. Kapcia, R. Lemanski a M. J. Zygmunt, „Extended Falicov-Kimball Model: Hartree--Fock vs DMFT approach," *Journal of Physics: Condensed Matter,* sv. 33, č. 6, p. 065602, 2020.

A Attachments

In this section, we present several simplified cases of the Falicov-Kimball model. In the attachment A.1, we consider the non-interacting case ($U = 0$). In the attachment A.2, we consider the case of a checkerboard staggered potential.

A.1 The non-interacting Falicov-Kimball model

If we assume a non-interacting case ($U = 0$), then the Hamiltonian from (1) changes to:

$$H_{FK} = -t \sum_{\langle i,j \rangle} \left(d_i^\dagger d_j + d_j^\dagger d_i \right), \tag{A1}$$

since the other term is zero.

We perform a canonical transformation on creation and annihilation operators:

$$c_{\boldsymbol{k}}^\dagger = \frac{1}{\sqrt{N}} \sum_{\boldsymbol{l}} e^{i\boldsymbol{k}\cdot\boldsymbol{l}} d_{\boldsymbol{l}}^\dagger, \tag{A2}$$

where $d_{\boldsymbol{l}}^\dagger$ is a creation operator in real space and $c_{\boldsymbol{k}}^\dagger$ is a creation operator in the momentum space.

We can use the following orthogonality identitites to invert (A2) and to rewrite the Hamiltonian (A1) in terms of operators from the momentum space [84]:

$$\frac{1}{N} \sum_l e^{i(k_m - k_n)l} = \delta_{m,n} \quad \text{and} \quad \frac{1}{N} \sum_n e^{ik_n(l-j)} = \delta_{l,j} \tag{A3}$$

To invert the equation for the creation operator in real space (A2), we first multiply both sides of the equation (A2) by $\frac{1}{\sqrt{N}}$ and by $e^{-i\boldsymbol{k}\cdot\boldsymbol{j}}$, then we sum both sides of the equation over $\boldsymbol{k}$ to get:

$$\frac{1}{\sqrt{N}} \sum_{\boldsymbol{k}} e^{-i\boldsymbol{k}\cdot\boldsymbol{j}} c_{\boldsymbol{k}}^\dagger = \frac{1}{N} \sum_{\boldsymbol{k}} \sum_{\boldsymbol{l}} e^{i\boldsymbol{k}\cdot(\boldsymbol{l}-\boldsymbol{j})} d_{\boldsymbol{l}}^\dagger \tag{A4}$$

We can reorganize terms on the right-hand side of the equation and use the second identity from (A3) to get:

$$\frac{1}{N} \sum_{\boldsymbol{k}} \sum_{\boldsymbol{l}} e^{i\boldsymbol{k}\cdot(\boldsymbol{l}-\boldsymbol{j})} d_{\boldsymbol{l}}^\dagger = \sum_{\boldsymbol{l}} \frac{1}{N} \sum_{\boldsymbol{k}} e^{i\boldsymbol{k}\cdot(\boldsymbol{l}-\boldsymbol{j})} d_{\boldsymbol{l}}^\dagger = \sum_{\boldsymbol{l}} \delta_{\boldsymbol{l},\boldsymbol{j}} d_{\boldsymbol{l}}^\dagger = d_{\boldsymbol{j}}^\dagger \tag{A5}$$

The inverted form of equation (A2) therefore is:

$$d_{\boldsymbol{j}}^\dagger = \frac{1}{\sqrt{N}} \sum_{\boldsymbol{k}} e^{-i\boldsymbol{k}\cdot\boldsymbol{j}} c_{\boldsymbol{k}}^\dagger \tag{A6}$$

Similarly, we can obtain a formula for the annihilation operator in real space by applying complex conjugation on the equation (A6).

$$d_j = \frac{1}{\sqrt{N}} \sum_{l} e^{il \cdot j} c_j \tag{A7}$$

Now, we can rewrite our Hamiltonian (A1) in terms of momentum operators. We will ignore the first term in the sum for now, because the formula for this term can be obtained by applying the complex conjugation to our formula for the second term, which we derive in the following text.

First, we substitute for our creation and annihilation operators $d_j^\dagger$ and d_i:

$$\sum_{\langle i,j \rangle} d_j^\dagger d_i = \sum_{\langle i,j \rangle} \frac{1}{\sqrt{N}} \sum_{k} e^{-ik \cdot j} c_k^\dagger \frac{1}{\sqrt{N}} \sum_{l} e^{il \cdot i} c_l \tag{A8}$$

Then, we use the fact that we are summing over nearest neighbors only, denoted by $\langle i, j \rangle$. We can instead sum over i and α, where α indicates we are summing over nearest neighbors. We are effectively making a substitution $j = i + \alpha$. We get:

$$\sum_{\langle i,j \rangle} d_j^\dagger d_i = \frac{1}{N} \sum_{i} \sum_{\alpha} \sum_{k} \sum_{l} e^{-ik \cdot i} e^{-ik \cdot \alpha} e^{il \cdot i} c_k^\dagger c_l \tag{A9}$$

We can reorganize our terms. When doing so, we write parentheses around the term on which the first identity from (A3) will be applied.

$$\sum_{\langle i,j \rangle} d_j^\dagger d_i = \sum_{\alpha} \sum_{k} \sum_{l} \left(\frac{1}{N} \sum_{i} e^{i(l-k) \cdot i} \right) e^{-ik \cdot \alpha} c_k^\dagger c_l \tag{A10}$$

Applying the identity and using properties of Kronecker delta we get:

$$\sum_{\langle i,j \rangle} d_i^\dagger d_j = \sum_{\alpha} \sum_{k} \sum_{l} \delta_{l,k} e^{-ik \cdot \alpha} c_k^\dagger c_l = \sum_{\alpha} \sum_{k} e^{-ik \cdot \alpha} c_k^\dagger c_k \tag{A11}$$

We can obtain similar expression for the sum of first term in Hamiltonian (A1):

$$\sum_{\langle i,j \rangle} d_j^\dagger d_i = \sum_{\alpha} \sum_{k} e^{ik \cdot \alpha} c_k^\dagger c_k \tag{A12}$$

Substituting for both sums in Hamiltonian (A1), we get:

$$\begin{aligned} H_{FK} &= -t \sum_{k} \sum_{\alpha} \left(e^{ik \cdot \alpha} + e^{-ik \cdot \alpha} \right) c_k^\dagger c_k \\ &= -2t \sum_{k} \sum_{\alpha} cos(k \cdot \alpha) c_k^\dagger c_k \end{aligned} \tag{A13}$$

Using the fact that α indicates we are summing over nearest neighbors, we can rewrite our Hamiltonian as a sum of cosines.

$$H_{FK} = -2t \sum_{k} \sum_{i=1}^{D} cos(k_i) c_k^\dagger c_k, \tag{A14}$$

where D is a dimension of the lattice.

We can also rewrite our Hamiltonian like this:

$$H_{FK} = \sum_{\boldsymbol{k}} \varepsilon_{\boldsymbol{k}} c_{\boldsymbol{k}}^{\dagger} c_{\boldsymbol{k}}, \tag{A15}$$

where

$$\varepsilon_{\boldsymbol{k}} = -2t \sum_{i=1}^{D} cos(k_i) \tag{A16}$$

The Hamiltonian (A15) can be written in a matrix form, if we replace the summation by integration and integrate over the Brillouine zone [47]:

$$H_{FK} = \prod_{i=2}^{D} \int_{-\pi}^{\pi} \frac{dk_i}{2\pi} \int_{-\frac{\pi}{2}}^{\frac{\pi}{2}} \frac{dk_1}{2\pi} \times \begin{pmatrix} c_{\boldsymbol{k}}^{\dagger} & c_{\boldsymbol{k}}^{\dagger} \end{pmatrix} \begin{pmatrix} \varepsilon_{\boldsymbol{k}} & 0 \\ 0 & \varepsilon_{\boldsymbol{k}} \end{pmatrix} \begin{pmatrix} c_{\boldsymbol{k}} \\ c_{\boldsymbol{k}} \end{pmatrix} \tag{A17}$$

From this form, it is clear that eigenvalues are:

$$\lambda_{\boldsymbol{k}} = \varepsilon_{\boldsymbol{k}} \tag{A18}$$

The eigenvalues are degenerate and two eigenvectors belong to each eigenvalue. These two eigenvectors are the same for each eigenvalue and look like this:

$$v_{\boldsymbol{k}}^{+} = \begin{pmatrix} 1 \\ 0 \end{pmatrix} \quad \text{and} \quad v_{\boldsymbol{k}}^{-} = \begin{pmatrix} 0 \\ 1 \end{pmatrix} \tag{A19}$$

A.2 The staggered potential for the Falicov-Kimball model

For the case of the checkerboard staggered potential, our Hamiltonian looks like this [84, 47]:

$$H_{FK} = -t \sum_{\langle i,j \rangle} \left(d_i^{\dagger} d_j + d_j^{\dagger} d_i \right) + \Delta \sum_{\boldsymbol{l}} (-1)^{\boldsymbol{l}} d_{\boldsymbol{l}}^{\dagger} d_{\boldsymbol{l}} \tag{A20}$$

We will again apply the same canonical transformation (A2) and express the Hamiltonian in terms of operators from the momentum space. Since the hopping term of Hamiltonian (A20), is the same as for the non-interacting case, this part of the Hamiltonian will be the same as in (A15).

Therefore, we only need to find the formula for the potential term of Hamiltonian (A20). Similarly as previously, we substitute for creation and annihilation operators from the real space using equations (A6) and (A7). We also rewrite -1 using imaginary exponential to get:

$$\Delta \sum_{\boldsymbol{l}} (-1)^{\boldsymbol{l}} d_{\boldsymbol{l}}^{\dagger} d_{\boldsymbol{l}} = \Delta \sum_{\boldsymbol{l}} e^{i\boldsymbol{\pi}\cdot\boldsymbol{l}} \frac{1}{\sqrt{N}} \sum_{\boldsymbol{k}} e^{-i\boldsymbol{k}\cdot\boldsymbol{l}} c_{\boldsymbol{k}}^{\dagger} \frac{1}{\sqrt{N}} \sum_{\boldsymbol{j}} e^{i\boldsymbol{j}\cdot\boldsymbol{l}} c_{\boldsymbol{j}} \tag{A21}$$

We reorder terms and write in parentheses the term, to which we apply the first identity from (A3).

$$\Delta \sum_{\boldsymbol{k}} \sum_{\boldsymbol{j}} \left(\frac{1}{N} \sum_{\boldsymbol{l}} e^{i(\boldsymbol{j}+\boldsymbol{\pi}-\boldsymbol{k})\cdot \boldsymbol{l}} \right) c_{\boldsymbol{k}}^{\dagger} c_{\boldsymbol{j}} \tag{A22}$$

Applying the identity and using properties of Kronecker delta we get:

$$\Delta \sum_{\boldsymbol{k}} \sum_{\boldsymbol{j}} \delta_{\boldsymbol{j}+\boldsymbol{\pi},\boldsymbol{k}} c_{\boldsymbol{k}}^{\dagger} c_{\boldsymbol{j}} = \Delta \sum_{\boldsymbol{k}} c_{\boldsymbol{k}}^{\dagger} c_{\boldsymbol{k}+\boldsymbol{\pi}} \tag{A23}$$

The Hamiltonian for staggered potential in terms of operators from the momentum space therefore is:

$$H_{FK} = \sum_{\boldsymbol{k}} \varepsilon_{\boldsymbol{k}} c_{\boldsymbol{k}}^{\dagger} c_{\boldsymbol{k}} + \Delta \sum_{\boldsymbol{k}} c_{\boldsymbol{k}}^{\dagger} c_{\boldsymbol{k}+\boldsymbol{\pi}} \tag{A24}$$

where $\varepsilon_{\boldsymbol{k}}$ is again given by (A16).

This Hamiltonian can be rewritten in a matrix form similar to Hamiltonian (A17) [47, 84]:

$$H_{FK} = \prod_{i=2}^{D} \int_{-\pi}^{\pi} \frac{dk_i}{2\pi} \int_{-\frac{\pi}{2}}^{\frac{\pi}{2}} \frac{dk_1}{2\pi} \times \begin{pmatrix} c_{\boldsymbol{k}}^{\dagger} & c_{\boldsymbol{k}+\boldsymbol{\pi}}^{\dagger} \end{pmatrix} \begin{pmatrix} \varepsilon_{\boldsymbol{k}} & \Delta \\ \Delta & \varepsilon_{\boldsymbol{k}+\boldsymbol{\pi}} \end{pmatrix} \begin{pmatrix} c_{\boldsymbol{k}} \\ c_{\boldsymbol{k}+\boldsymbol{\pi}} \end{pmatrix} \tag{A25}$$

From the matrix form, we can easily find eigenvalues. When doing so, we utilize the following identity:

$$cos(k+\pi) = -cos(k) \tag{A26}$$

The eigenvalues are:

$$\lambda_{\boldsymbol{k}}^{\pm} = \pm \sqrt{\varepsilon_{\boldsymbol{k}}^2 + \Delta^2} \tag{A27}$$

The corresponding orthonormal eigenvectors are:

$$v_{\boldsymbol{k}}^{+} = \begin{pmatrix} \frac{\varepsilon_{\boldsymbol{k}} + \sqrt{\varepsilon_{\boldsymbol{k}}^2 + \Delta^2}}{\sqrt{\Delta^2 + \left(\varepsilon_{\boldsymbol{k}} + \sqrt{\varepsilon_{\boldsymbol{k}}^2 + \Delta^2} \right)^2}} \\ \frac{\Delta}{\sqrt{\Delta^2 + \left(\varepsilon_{\boldsymbol{k}} + \sqrt{\varepsilon_{\boldsymbol{k}}^2 + \Delta^2} \right)^2}} \end{pmatrix} \quad \text{and} \quad v_{\boldsymbol{k}}^{-} = \begin{pmatrix} \frac{\varepsilon_{\boldsymbol{k}} - \sqrt{\varepsilon_{\boldsymbol{k}}^2 + \Delta^2}}{\sqrt{\Delta^2 + \left(\varepsilon_{\boldsymbol{k}} - \sqrt{\varepsilon_{\boldsymbol{k}}^2 + \Delta^2} \right)^2}} \\ \frac{\Delta}{\sqrt{\Delta^2 + \left(\varepsilon_{\boldsymbol{k}} - \sqrt{\varepsilon_{\boldsymbol{k}}^2 + \Delta^2} \right)^2}} \end{pmatrix} \tag{A28}$$